CHEMISTRY OF MATERIALS

pubs.acs.org/cm

Article

$ACuZrQ_3$ (A = Rb, Cs; Q = S, Se, Te): Direct Bandgap Semiconductors and Metals with Ultralow Thermal Conductivity

Craig C. Laing, Benjamin E. Weiss, Koushik Pal, Michael A. Quintero, Hongyao Xie, Xiuquan Zhou, Jiahong Shen, Duck Young Chung, Christopher Wolverton, and Mercouri G. Kanatzidis*

Cite This: *Chem. Mater.* 2022, 34, 8389−8402

Read Online

ACCESS | Metrics & More | Article Recommendations | Supporting Information

ABSTRACT: $ACuZrQ_3$ (A = Rb, Cs; Q = S, Se, Te) were synthesized as black platelet crystals. $RbCuZrS_3$, $RbCuZrSe_3$, and $CsCuZrS_3$ crystallize in the $KCuZrSe_3$ structure type with space group *Cmcm*, and $RbCuZrTe_3$ and $CsCuZrTe_3$ crystallize in the lower symmetry space group *Pnma*. The tellurides exhibit a second-order Jahn−Teller distortion with off-centering of Zr in its octahedral environment. The magnitude of the distortion is larger in $RbCuZrTe_3$ than in $CsCuZrTe_3$. The structures of β-$CsCuS_4$ and $Rb_2Cu_5Te_5$ were also determined. $CsCuZrS_3$ melts at 910 °C and exhibits partial decomposition upon heating at 275 °C, while $CsCuZrTe_3$ melts incongruently. Our DFT calculations of $RbCuZrQ_3$ (Q = S, Se) and $CsCuZrS_3$ indicate direct gap semiconductors in agreement with experiments. $ACuZrTe_3$ (A = Rb, Cs) were calculated to be metals which was confirmed for $RbCuZrTe_3$ with variable temperature conductivity measurements and consistent with heat capacity measurements. Spectroscopic measurements found a bandgap and work function of 1.44(5) eV and 4.89(5) eV for $RbCuZrS_3$ and 0.95(5) eV and 4.67(5) eV for $RbCuZrSe_3$, respectively. $RbCuZrTe_3$ did not exhibit an optical bandgap and has a work function of 4.64(5) eV. $RbCuZrTe_3$ exhibits a low thermal conductivity under 0.5 W m^{-1} K^{-1} at room temperature.

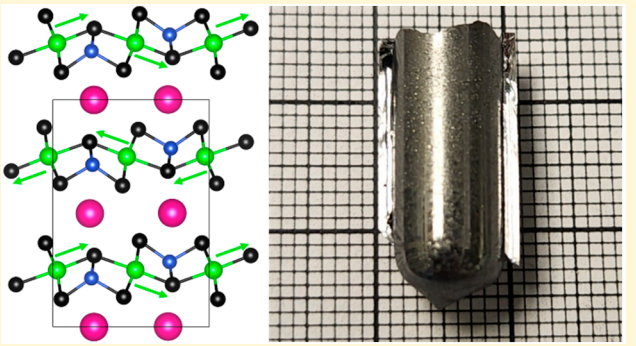

INTRODUCTION

Quaternary chalcogenides ACuMQ (A = alkali metal, M = metal, Q = chalcogen) are part of a large family encompassing a variety of structure types and compositions. Many of the known materials exhibit layered structures, such as $KCuMnSe_2$,[1] $Cs_2Cu_2Cd_2S_4$,[2] and $KCuLa_2S_6$,[3] while others exhibit three-dimensional (3D) structures such as $Li_{1.66}CuSn_{3.33}S_8$[4] and $Rb_2CuSb_7S_{12}$.[5] These materials exhibit properties including magnetism, photocurrent response,[2,5] exfoliation,[3] and lithium ion conductivity.[4] Recent theoretical works[6−8] have examined materials with the $AMM'Q_3$ stoichiometry in the several possible structure types and predicted new compositions that should be stable with low thermal conductivity ideal for thermoelectrics. Moreover, $KCuZrQ_3$ (Q = S, Se, Te) in the $KCuZrSe_3$ structure type were reported to have unusual charge transport properties.[9] Other compositions also adopt the interesting $KCuZrSe_3$ structure type, including $Ba_{0.5}CuYSe_3$[10] and $CsGdZnSe_3$.[11] The high stability and predicted low thermal conductivity of the $KCuZrSe_3$ structure type and the unusual charge transport properties of the $KCuZrQ_3$ members collectively motivated this study to explore the heavier alkali metals analogues of $ACuZrQ_3$ (A = Rb, Cs; Q = S, Se, Te) as only $CsCuZrSe_3$ had previously been reported.

Herein we report the synthesis, structure, and properties of $RbCuZrQ_3$ (Q = S, Se, Te), $CsCuZrS_3$, and $CsCuZrTe_3$ as well as the structure of the new compounds β-$CsCuS_4$ and $Rb_2Cu_5Te_5$ found as side products. $RbCuZrS_3$, $RbCuZrSe_3$, and $CsCuZrS_3$ crystallize in the $KCuZrSe_3$ structure type in the space group *Cmcm* while $RbCuZrTe_3$ and $CsCuZrTe_3$ crystallize in a distorted version of the structure type in the space group *Pnma*. The distortion is due to the d^0 Zr exhibiting second-order Jahn−Teller distortion. The magnitude of this distortion is larger for $RbCuZrTe_3$ than for $CsCuZrTe_3$ and was found to increase for $RbCuZrTe_3$ upon cooling from 293 to 100 K. Density functional theory (DFT) calculations predict $RbCuZrQ_3$ (Q = S, Se) and $CsCuZrS_3$ to be direct gap semiconductors. In contrast, $ACuZrTe_3$ (A = Rb, Cs) are predicted to be metallic. $RbCuZrTe_3$ was confirmed to be a metal with variable temperature conductivity measurements. Low-temperature heat capacity measurements also suggest that

Received: July 12, 2022
Revised: August 29, 2022
Published: September 14, 2022

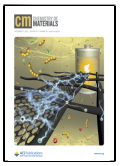

both $RbCuZrTe_3$ and $CsCuZrTe_3$ are metals with positive heat capacity γ values and Debye temperatures of 150 and 170 K, respectively. Spectroscopic measurements find a bandgap and work function of 1.44(5) eV and 4.89(5) eV for $RbCuZrS_3$ and 0.95(5) eV and 4.67(5) eV for $RbCuZrSe_3$, while no optical bandgap was observed for $RbCuZrTe_3$ with a work function of 4.64(5) eV. $RbCuZrTe_3$ was found to exhibit very low thermal conductivity just below 0.5 W m^{-1} K^{-1} at room temperature, falling to 0.35 W m^{-1} K^{-1} at 575 K.

EXPERIMENTAL METHODS

Reagents. Cs (99.5%, Alfa Aesar), Rb (99.5% Alfa Aesar), S (99.99%, 5N Plus Inc.), Se (99.99%, American Elements), Te (99.999% American Elements), CuS (99.99%, Sigma-Aldrich), Zr (99.95% Alfa Aesar), CsCl (99.9%, Alfa Aesar), and RbCl (99.9%, Alfa Aesar) were used as purchased without additional purification. Cu (99.7%, MilliporeSigma) powder was activated by washing with 10 wt % HCl followed by a deionized water rinse and dried with isopropanol in a vacuum filter and stored in a glovebox.

Synthesis of A_xQ_y. Amounts of ~15 g batches of A_xQ_y (A = Rb, Cs; Q = S, Se, Te) were prepared from stoichiometric reactions of the two respective elements in liquid ammonia NH_3 as described previously.[12,13] A typical synthesis is as follows: Cs or Rb metal was slightly heated (~30 or ~40 °C, respectively) and pipetted into a 250 mL three-neck round-bottom flask with a glass stir bar and a Teflon valve in a nitrogen glovebox. The airtight flask was then transferred out of the box to a Schlenk line. The line was then purged with nitrogen, and then 150 mL of ammonia gas was condensed into the flask at −77 °C with a dry ice/acetone bath and allowed to dissolve the alkali metal which formed a dark blue solution for about 1 h. The chalcogen was added to the mixture and stirred for several hours. The ammonia was then allowed to evaporate under a nitrogen flow by allowing the dry ice/acetone bath to warm up to room temperature. The air-sensitive material was then dried via vacuum overnight and stored in a glovebox. Rb_2S and Cs_2S were white/pale yellow. Rb_2Se was white/pale orange. Rb_2Te_2 and Cs_2Te_2 appeared black (probably because of the presence of longer Te_x^{2-}, $x > 2$, impurities). Cs_2S_4 was orange.

Synthesis of $RbCuZrQ_3$. $RbCuZrQ_3$ crystals suitable for single crystal X-ray diffraction were synthesized by using a combination of Rb_2Q_x (Q = S, Se and $x = 1$; Q = Te and $x = 2$), Cu or CuS, Zr, and either S, Se, or Te in a stoichiometric ratio. This mixture was then combined with RbCl in either a 1:7 ratio when Q = S or a 1:10 ratio when Q = Se or Te. For $RbCuZrS_3$ the reagents Rb_2S (0.120 g, 0.591 mmol), CuS (0.113 g, 1.18 mmol), Zr (0.108 g, 1.18 mmol), S (0.057 g, 1.8 mmol), and RbCl (1.002 g, 8.286 mmol) were combined in a 1:2:2:3:14 ratio of Rb_2S:CuS:Zr:S:RbCl. For $RbCuZrSe_3$ the reagents Rb_2Se (0.104 g, 0.416 mmol), Cu (0.053 g, 0.83 mmol), Zr (0.076 g, 0.83 mmol), Se (0.164 g, 2.08 mmol), and RbCl (1.004 g, 8.303 mmol) were combined in a 1:2:2:5:20 ratio of Rb_2Se:Cu:Zr:Se:RbCl. For $RbCuZrTe_3$ the reagents Rb_2Te_2 (0.163 g, 0.383 mmol), Cu (0.049 g, 0.77 mmol), Zr (0.070 g, 0.77 mmol), Te (0.195 g, 1.53 mmol), and RbCl (0.924 g, 7.64 mmol) were combined in a 1:2:2:4:20 molar ratio of Rb_2Te_2:Cu:Zr:Te:RbCl. The mixture was prepared in a nitrogen glovebox and was homogenized with a mortar and pestle. Fused silica tubes with outer diameter (OD) 13 mm and inner diameter (ID) 11 mm lined with aluminum foil to prevent powder from sticking to the sides were charged with the respective mixture. The tube was then transferred to a vacuum line, evacuated to 2.9×10^{-3} mbar, and then flame-sealed with a torch. The sealed tube was then placed inside a ceramic mullite tube inside of a programmable one-zone tube furnace packed with insulation wool. The tube was positioned such that the top of the tube was in the hot center of the tube furnace while the end with the reagents was adjacent to the thermocouple closer to the bottom of the furnace to suppress volatilization. The furnace was heated to 800 °C in 15 h and held at this temperature for 24 h. For $RbCuZrTe_3$ the furnace was turned off and allowed to cool to room temperature. For $RbCuZrS_3$ and $RbCuZrSe_3$ the furnace was cooled at 4 °C/h to 600 °C, and then the furnace was turned off and allowed to cool to room temperature. $RbCuZrQ_3$ (Q = S, Se, Te) in the form of black platelet crystals were mechanically separated for single-crystal X-ray diffraction.

Synthesis of $CsCuZrS_3$. $CsCuZrS_3$ was synthesized by using a CsCl flux to produce pure bulk material. $CsCuZrS_3$ was synthesized by using Cs_2S_4 (0.205 g, 0.520 mmol), CuS (0.100 g, 1.05 mmol), Zr (0.095 g, 1.04 mmol), and CsCl (1.000 g, 5.940 mmol) combined in a 1:2:2:5.657 molar ratio of Cs_2S_4:CuS:Zr:CsCl. The mixture was prepared in a nitrogen glovebox and was homogenized with a mortar and pestle. A fused silica tube with an OD of 13 mm and an ID of 11 mm lined with aluminum foil to prevent powder from sticking to the sides was charged with the mixture. The tube was then transferred to a vacuum line, evacuated to 2.9×10^{-3} mbar, and then flame-sealed with a torch. The sealed tube was then placed inside a mullite tube in a programmable one-zone tube furnace which was then packed with insulation wool. To suppress any volatilization during the reaction, the tube was positioned such that the end with the reagents was adjacent to the thermocouple and the top of the tube was just below the center of the tube furnace, which is the hottest region of the furnace. The furnace was heated to 700 °C at a rate of 20 °C/h, dwelled for 24 h, and then the furnace was turned off and allowed to cool to room temperature. The tube was opened in a fume hood, and the material was ground and homogenized. The homogeneous mixture was then charged into a new fused silica tube with the same dimensions and flame-sealed under vacuum in the same manner. The tube was then placed into the same furnace in an identical manner. The furnace was then heated to 300 °C at a rate of 20 °C/h. The heating rate was then increased to 100 °C/h until it reached a temperature of 1000 °C and then dwelled for 6 h. The furnace was then turned off and allowed to cool to room temperature. Black platelet crystals, clear crystals, and red irregularly shaped crystals were observed. The product was then washed sequentially with deionized water, methanol, and dimethylformamide, removing the clear and red crystals. The remaining black platelets were then dried by a rinse of methanol followed by nitrogen gas until the methanol had evaporated. Pictures of the crystals are presented in the Supporting Information (Figure S14).

Synthesis of $ACuZrTe_3$. A 5.5 g ingot of $CsCuZrTe_3$ was synthesized by stoichiometric combination by using Cs_2Te_2 (2.137 g, 4.102 mmol), Cu (0.521 g, 8.20 mmol), Zr (0.748 g, 8.20 mmol), and Te (2.093 g, 16.41 mmol) combined in a 1:2:2:4 molar ratio of Cs_2Te_2:Cu:Zr:Te. A 5.5 g ingot of $RbCuZrTe_3$ was synthesized by stoichiometric combination by using Rb_2Te_2 (1.881 g, 4.414 mmol), Cu (0.561 g, 8.83 mmol), Zr (0.805 g, 8.83 mmol), and Te (2.253 g, 17.66 mmol) combined in a 1:2:2:4 molar ratio of Rb_2Te_2:Cu:Zr:Te. The mixtures were prepared in a nitrogen glovebox and were homogenized with a mortar and pestle. Fused silica tubes with an OD of 10 mm and an ID of 8 mm lined with aluminum foil to prevent powder from sticking to the sides were charged with the mixture. The tube was then transferred to a vacuum line, evacuated to 2.9×10^{-3} mbar, and then flame-sealed with a torch with an internal length of 20 cm. The sealed tube was then placed inside a mullite tube in a programmable one-zone tube furnace which was then packed with insulation wool. To suppress volatilization during the reaction, the tube was positioned such that the end with the reagents was adjacent to the thermocouple and the top of the tube was just below the center of the tube furnace, which is the hottest region of the furnace. The furnace was heated to 1000 °C at a rate of 100 °C/h, dwelled for 12 h, and then water quenched. The tubes were opened in a fume hood, and black ingots with metallic luster were obtained.

Single-Crystal X-ray Diffraction. Intensity data of suitable platelet-shaped single crystals were mounted on a glass fiber with super glue and diffracted on either a STOE IPDS 2, STOE IPDS 2T, or STOE StadiVari diffractometer at 293 K. The STOE IPDS 2 and STOE IPDS 2T diffractometers were equipped with Mo Kα (λ = 0.71073 Å) sealed X-ray source with X-ray fiber optics and an image plate detector. The STOE StadiVari diffractometer was equipped with an AXO Auxilia Microfocus Ag Kα (λ = 0.56083 Å) sealed X-ray source and a Dectris Pilatus3 R CdTe 300K Hybrid Photon Counting detector. Data reduction was performed with the STOE X-Area ver.

https://doi.org/10.1021/acs.chemmater.2c02104
Chem. Mater. 2022, 34, 8389−8402

Table 1. Select Crystal Data and Structure Refinements for $RbCuZrQ_3$ Compounds[a]

empirical formula	$RbCuZrS_3$	$RbCuZrSe_3$	$RbCuZrTe_3$	$RbCuZrTe_3$
formula weight	672.82	954.22	1246.06	1246.06
temperature	293 K	293 K	293 K	100 K
wavelength	0.71073 Å	0.56083 Å	0.56083 Å	0.56083 Å
crystal system	orthorhombic	orthorhombic	orthorhombic	orthorhombic
space group	*Cmcm*	*Cmcm*	*Pnma*	*Pnma*
unit cell dimensions	a = 3.7597(8) Å	a = 3.8954(8)	a = 10.951(2) Å	a = 10.970(2) Å
	b = 14.621(3) Å	b = 15.147(3)	b = 4.1342(8) Å	b = 4.1198(8) Å
	c = 9.813(2) Å	c = 10.193(2) Å	c = 16.074(3) Å	c = 15.905(3) Å
	$\alpha = \beta = \gamma$ = 90°	$\alpha = \beta = \gamma$ = 90°	$\alpha = \beta = \gamma$ = 90°	$\alpha = \beta = \gamma$ = 90°
volume	539.42(19) Å^3	601.4(2) Å^3	727.8(2) Å^3	718.8(2) Å^3
density (calculated)	4.142 g/cm^3	5.269 g/cm^3	5.686 g/cm^3	5.757 g/cm^3
independent reflections	489	1080	2224	1967
	[R_{int} = 0.0509]	[R_{int} = 0.0146]	[R_{int} = 0.0194]	[R_{int} = 0.0320]
goodness-of-fit	1.036	1.136	1.030	1.088
final R indices [$I > 2\sigma(I)$]	R_{obs} = 0.0600	R_{obs} = 0.0288	R_{obs} = 0.0242	R_{obs} = 0.0512
	wR_{obs} = 0.1555	wR_{obs} = 0.0786	wR_{obs} = 0.0572	wR_{obs} = 0.1432
R indices [all data]	R_{all} = 0.0711	R_{all} = 0.0319	R_{all} = 0.0333	R_{all} = 0.0519
	wR_{all} = 0.1659	wR_{all} = 0.0815	wR_{all} = 0.0600	wR_{all} = 0.1444

[a] $R = \sum||F_o| - |F_c||/\sum|F_o|$, $wR = \{\sum[w(|F_o|^2 - |F_c|^2)^2]/\sum[w(|F_o|^4)]\}^{1/2}$, and $w = 1/[\sigma^2(F_o^2) + (P)^2]$ where $P = (F_o^2 + 2F_c^2)/3$.

Table 2. Select Crystal Data and Structure Refinements for Cs Compounds and $Rb_2Cu_5Te_5$[a]

empirical formula	$CsCuZrS_3$	$CsCuZrTe_3$	β-$CsCuS_4$	$Rb_2Cu_5Te_5$
formula weight	767.70	1340.94	324.69	2253.28
temperature	293 K	293 K	293 K	293 K
wavelength	0.71073 Å	0.56083 Å	0.71073 Å	0.56083 Å
crystal system	orthorhombic	orthorhombic	triclinic	orthorhombic
space group	*Cmcm*	*Pnma*	$P\bar{1}$	*Cmcm*
unit cell dimensions	a = 3.7813(8) Å	a = 10.9494(7) Å	a = 5.4526(2) Å	a = 4.1576(8) Å
	b = 15.347(3) Å	b = 4.1363(3) Å	b = 7.2673(4) Å	b = 16.426(3) Å
	c = 9.848(2) Å	c = 16.9039(18) Å	c = 9.2050(6) Å	c = 18.661(4) Å
	$\alpha = \beta = \gamma$ = 90°	$\alpha = \beta = \gamma$ = 90°	α = 105.242(5)°	$\alpha = \beta = \gamma$ = 90°
			β = 96.936(4)°	
			γ = 110.478(4)°	
volume	571.5(2) Å^3	765.58(11) Å^3	320.42(3) Å^3	1274.4(4) Å^3
density (calculated)	4.461 g/cm^3	5.817 g/cm^3	3.365 g/cm^3	5.872 g/cm^3
independent reflections	318	1351	1705	1746
	[R_{int} = 0.0614]	[R_{int} = 0.0351]	[R_{int} = 0.0570]	[R_{int} = 0.0251]
goodness-of-fit	1.061	1.052	1.142	1.074
final R indices [$I > 2\sigma(I)$]	R_{obs} = 0.0914	R_{obs} = 0.0465	R_{obs} = 0.0726	R_{obs} = 0.0273
	wR_{obs} = 0.2246	wR_{obs} = 0.1176	wR_{obs} = 0.2067	wR_{obs} = 0.0759
R indices [all data]	R_{all} = 0.1214	R_{all} = 0.0767	R_{all} = 0.0788	R_{all} = 0.0280
	wR_{all} = 0.2592	wR_{all} = 0.1337	wR_{all} = 0.2111	wR_{all} = 0.0766

[a] $R = \sum||F_o| - |F_c||/\sum|F_o|$, $wR = \{\sum[w(|F_o|^2 - |F_c|^2)^2]/\sum[w(|F_o|^4)]\}^{1/2}$, and $w = 1/[\sigma^2(F_o^2) + (P)^2]$ where $P = (F_o^2 + 2F_c^2)/3$.

1.90 software package. A numerical absorption correction was applied by using STOE X-Red ver. 1.65.2 and STOE X-Shape ver. 2.21 followed by scaling and outlier rejection with STOE LANA ver. 1.83.8.[14] The structure was solved with the ShelXT intrinsic phasing solution method[15] and was refined with ShelXL full-matrix least-squares minimization on the F^2 method.[16] Olex2[17] was used as the graphical interface. Select crystallographic information can be found in Tables 1 and 2 with complete crystallographic information found in Tables S1−S34.

Electronic Structure and Phonon Dispersion Calculations. We performed first-principles calculations based on density functional theory (DFT)[18,19] using the Vienna Ab initio Simulation Package (VASP)[20,21] along with potentials of the elements derived by using the projector augmented-wave (PAW)[22] method. We used the following PAW potentials for Rb ($4s^2\ 4p^6\ 5s^1$), Cs ($5s^2\ 5p^6\ 6s^1$), Cu ($3d^{10}\ 4s^1$), Zr ($4s^2\ 4p^6\ 4d^2\ 5s^2$), S ($3s^2\ 3p^4$), Se ($4s^2\ 4p^4$), and Te ($5s^2\ 5p^4$) in our calculations. The Perdew−Burke−Ernzerhof (or PBEsol)[23] exchange-correlation energy functional for solids was employed in all calculations. We used 8000 k-points per reciprocal atom (KPPRA) for optimization of the unit cells. The plane wave basis set with cutoff energy of 520 eV was adopted. The crystal structures were fully relaxed until the total energy converged to 10^{-8} eV, and the force on each atom is less than 0.001 eV/Å. The optimized lattice constants of $CsCuZrS_3$ (experiment: a = 3.781 Å, b = 15.347 Å, c = 9.848 Å; calculated: a = 3.735 Å, b = 15.255 Å, c = 9.720 Å), $CsCuZrTe_3$ (experiment: a = 10.949 Å, b = 4.136 Å, c = 16.904 Å; calculated: a = 10.976 Å, b = 4.088 Å, c = 16.736 Å), $RbCuZrS_3$ (experiment: a = 3.760 Å, b = 14.621 Å, c = 9.813 Å; calculated: a = 3.719 Å, b = 14.584 Å, c = 9.700 Å), $RbCuZrSe_3$ (experiment: a = 3.895 Å, b = 15.147 Å, c = 10.193 Å; calculated: a = 3.858 Å, b = 15.196 Å, c = 10.088 Å), and $RbCuZrTe_3$ (experiment: a = 10.951 Å, b = 4.134 Å, c = 16.074 Å; calculated:, a = 10.967 Å, b = 4.077 Å, c = 16.019 Å) agree very well with the corresponding experimental values. $RbCuZrTe_3$ and $CsCuZrTe_3$ have a *Pnma* space

https://doi.org/10.1021/acs.chemmater.2c02104
Chem. Mater. 2022, 34, 8389−8402

group (No. 62) and contains 24 atoms in the primitive unit cell whereas the rest of the quaternary compounds have the *Cmcm* space group (No. 63) and contain 12 atoms in their primitive unit cell. For the convenience of the calculations, we rearranged the lattice vectors of $RbCuZrTe_3$ and $CsCuZrTe_3$ such that $a < b < c$ without changing the symmetries of their lattices. The spin−orbit coupling was included while calculating the electronic band structures of the compounds. We performed phonon calculations using the PHONOPY package[24] that utilized a finite displacement supercell method for the calculation of forces and construction of the second-order interatomic force constant matrices from the force−displacement data. For the sulfide and selenide compounds having *Cmcm* symmetry we used ([2, 0, 0], [0, 2, 0], [0, 0, 1]) supercell transformation matrix to generate the displaced supercells. Each supercell of the compounds having *Cmcm* space group contains 48 atoms, and we used a 5 × 5 × 7 k-point mesh for the calculation of forces on the atoms. On the other hand, we used ([1,1,1], [1,0,1], [3,1,0]) and ([0,1,1], [3,0,1], [3,1,0]) supercell transformation matrices respectively for $RbCuZrTe_3$ and $CsCuZrTe_3$ to generate relatively isotropic supercells. Each supercell of $RbCuZrTe_3$ has 72 atoms, and we used a 4 × 4 × 4 k-point mesh to calculate the forces on the atoms. For $CsCuZrTe_3$, each supercell contains 144 atoms, and a 2 × 2 × 2 k-point mesh was used for force calculations. We performed the crystal orbital Hamilton population (COHP) analysis using the LOBSTER code,[25,26] which can identify the nature of interactions (i.e., bonding, nonbonding and antibonding states) between the atoms. The COHP analysis does not include spin−orbit coupling.

Thermoelectric Property Measurements. The $RbCuZrTe_3$ crystals were crushed and hand-ground into a fine powder and sintered via the spark plasma sintering (SPS) apparatus at 623 K under a pressure of 40 MPa in a vacuum for 5 min to obtain a densified bulk sample (φ 12.7 × 3.5 mm^2, density = 5.0588 g cm^{-3}). The SPSed sample was then cut and polished into a 3 × 3 × 10 mm^3 rectangular bar for electronic transport properties measurement and a 6 × 6 × 1.5 mm^3 piece for thermal conductivity measurement. The high-temperature electrical conductivity (σ) and the Seebeck coefficient (S) were simultaneously measured by using a four-probe setup in a commercial apparatus (ZEM-3, Ulvac Riko, Inc.) under a He atmosphere from 300 to 575 K. The sample was measured under two heating processes and one cooling process (labeled as heat 1, heat 2, and cool 1; see the Supporting Information); the transport properties are very similar for both the heating and cooling cycles, indicating the sample is thermostable. The thermal conductivity was calculated by using the thermal diffusivity (D), heat capacity (C_p), and sample density (ρ) according to the relationship $\kappa = DC_p\rho$. The thermal diffusivity was measured in an Ar atmosphere by the laser flash diffusivity method (LFA 457; Netzsch). The heat capacity was calculated by the Dulong−Petit law, and the sample density was determined by measuring the mass and dimensions of the sample. We estimated the lattice thermal conductivity simply by subtracting the electronic thermal conductivity from the measured total thermal conductivity: $\kappa_L = \kappa_{total} - \kappa_{ele} = \kappa_{total} - L\sigma T$, where κ_L, κ_{total}, and κ_{ele} are the lattice thermal conductivity, total thermal conductivity, and electronic thermal conductivity, respectively. The latter can be estimated by the Wiedemann−Franz relation $\kappa_{ele} = L\sigma T$, where σ is the electrical conductivity and L is the Lorenz number.

RESULTS AND DISCUSSION

Synthesis and Crystal Growth. For the synthesis of $ACuZrS_3$ (A = Rb, Cs) careful consideration of the starting materials is needed to avoid undesired exothermic reactions before the reagents can be sealed under vacuum. Using activated copper powder and sulfur can cause a reaction upon grinding in a mortar and pestle, resulting in sulfur loss due to volatilization.[27] This can be avoided by using a copper sulfide binary as a starting material or by sealing and heating an unmixed Cu and S in a known stoichiometry and then grinding and homogenizing the reaction product. Such a mixture can then be treated as a Cu and S source with known stoichiometry without volatilizing sulfur and losing stoichiometric control. Moreover, synthetic attempts using Cs_2S or Rb_2S and S as starting materials (mainly when also using activated Cu, but not exclusively) resulted in exothermic reactions occurring either while evacuating the tube of air or during the silica flame-sealing step. A picture of this is shown in Figure S1. Cooling the silica tubes containing the starting materials with liquid nitrogen just after beginning to evacuate them and after some of the air has left the tube allows for most of the moisture in the air to leave and subsequently reduced the reactivity of the starting materials enough to avoid this exothermic event. In the case when activated Cu, S, and Cs_2S were used and successfully sealed, an exothermic event inside the sealed tube upon initial heating in the furnace that dispersed the starting material throughout the inside of the reaction tube upon heating would still occur, preventing a homogeneous reaction mixture with stoichiometric control at the bottom of the tube. Ultimately, the use of Cs_2S_4 and CuS for preparing $CsCuZrS_3$ was found to be the optimal to avoid these challenges. The use of Rb_2S and CuS was sufficient for preparing $RbCuZrS_3$ when care was taken during preparation.

Single crystals were grown and mechanically separated for structure determination using either RbCl or CsCl as a salt flux for $RbCuZrQ_3$ or $CsCuZrS_3$, respectively, with the following reaction as an example: $Rb_2Se + 2Cu + 2Zr + 5Se + 20RbCl \rightarrow 2RbCuZrSe_3 + 20RbCl$. In the case of $ACuZrS_3$ reactions, red side products were observed. For the Cs/S reaction, this red side product was identified as the new phase β-$CsCuS_4$ which crystallized in irregular shapes. β-$CsCuS_4$ is found to be soluble in water and in *N*,*N*-dimethylformamide (DMF). A bright blue color is observed when dissolved in DMF, characteristic of a solubilized polysulfide.[28] β-$CsCuS_4$ is a salt containing Cs^+ cations and $[CuS_4]^-$ polymeric anionics, which includes S_4^{2-} ligands bonding to copper atoms, so the solubility of this phase in polar solvents and the blue polysulfide color in DMF is expected and reasonable. A picture of the blue DMF solution can be found in Figure S2. In the case of the Rb-containing reaction targeting $RbCuZrS_3$, a suitable crystal could not be selected, so the side product could not be identified. The same blue color was still found in DMF, indicating the presence of a polysulfide which suggests likely a similar $RbCuS_4$ or $RbCuS_6$ polysulfide phase. In the $RbCuZrTe_3$/RbCl salt flux reaction, the side product $Rb_2Cu_5Te_5$ was identified as black platelets that had a triangular shape instead of the more typical rectangular shape observed for $RbCuZrTe_3$ crystals. Washing the product from this reaction with DMF did not result in any color changes to the DMF. Optimized synthesis conditions for either pure bulk material or large crystals that were washed and mechanically separated were ultimately achieved for all five of the ACuZrQ3 materials reported here without using ACl (A = Rb, Cs) salt fluxes. This is detailed in the Experimental Methods section or the additional experimental details in the Supporting Information.

Attempts to scale up the bulk synthesis of $RbCuZrSe_3$ and $ACuZrTe_3$ (A = Rb, Cs) through a stoichiometric combination of A_2Q_x, Cu, Zr, and Q to 4 g or more presented challenges and required careful consideration due to tube failure. An ∼1 g reaction run in fused silica tubes sealed to be 10 cm long (or 12 cm for $RbCuZrSe_3$) with an inner diameter of 8 mm and outer diameter of 10 mm placed vertically in the tube furnace typically resulted in some black material dispersed throughout the tube including at the top. A picture of this for $RbCuZrSe_3$

https://doi.org/10.1021/acs.chemmater.2c02104
Chem. Mater. 2022, 34, 8389−8402

is shown in Figure S3. Scaled-up reactions to 4 g resulted in the tubes breaking only at the top end with the rest of the silica tube intact (see photo in Figure S4). This indicates that the reactions are sufficiently exothermic upon heating to disperse or expand the material throughout the tube with enough force to break off the top of it when insufficient headspace in the tube is provided. In the case of $ACuZrTe_3$ (A = Rb, Cs), this was addressed by doubling the length of the tube to 20 cm long, which reproducibly survived for 5.5 g reactions. A 4 g reaction targeting $RbCuZrSe_3$ with a 15 cm long tube failed, and no successful scaled-up reaction conditions have been tested.

On the basis of experience in preparing these alkali metal containing chalcogenides, we can come to some useful guidelines for the preparation of these materials as well as other alkali metal containing chalcogenides that demonstrate substantial exothermic behavior. In general, the exothermic nature and the synthetic challenges associated with this follow the trend we would expect based on oxidizing power of the chalcogen where S > Se > Te. Liquid nitrogen cooling (after the evacuation process has started) lowers the reactivity of the starting materials and avoids reactions during the flame-sealing process, as observed for the sulfides. Reaction sizes below 1 g during exploratory stages or attempts to obtain suitable single crystals for structure determination reduce the chance of tubes breaking. Scaled-up reactions require larger tubes with additional head space to allow dispersed material to move without breaking the tube.

For a specific system, the identification of plausible reaction steps that could be responsible for the exotherm can enable the choice of starting materials that avoid or minimize this effect. A_xQ_y is prepared via the liquid ammonia reaction method[12,13] to prevent the exothermic reaction of an alkali metal with chalcogen, while the reaction of A_xQ_y + Q can be performed on the gram scale without strong exothermic events. Use of sulfur-rich A_xQ_y and CuS avoids any exotherm associated with the reduction of sulfur. The large exotherm occurring during the preparation of the $ACuZrS_3$ phases is likely due to a three-component reaction since the reaction of sulfur with either copper or zirconium is not sufficiently exothermic. The formation of S_4^{2-} anions from the reaction of A_2S + 3S in the presence of Cu could form the 1D polymeric $[CuS_4]^-$ chains of side product β-$CsCuS_4$ which would be highly exothermic. Using Cs_2S_4 where the S_4^{2-} anions are already formed with CuS or ternary phase starting materials to prepare quaternary phases can reduce the magnitude of the exotherm making the formation of these phases more manageable.

Crystal Structure. The new compounds $RbCuZrS_3$, $RbCuZrSe_3$, and $CsCuZrS_3$ are isostructural and adopt the $KCuZrSe_3$ structure type[9] with the space group *Cmcm* shown in Figure 1. This structure comprises $[CuZrQ_3]^-$ layers built from CuQ_4 tetrahedra and ZrQ_6 octahedra, which alternate with layers of alkali metal cations that serve to both fill the voids between $[CuZrQ_3]^-$ layers and charge-balance the structure. Each alkali metal atom forms undistorted eight-coordinate AQ_8 polyhedra. The $[CuZrQ_3]^-$ layers are composed of parallel infinite columns of CuQ_4 tetrahedra and ZrQ_6 octahedra that extend along the *a*-axis direction. The columns alternate along the *c*-axis direction (CuQ_4-ZrQ_6-CuQ_4-ZrQ_6). Each ZrQ_6 octahedron is edge-sharing with four adjacent CuQ_4 tetrahedra (two on each side) extending in the *c* direction and is also edge-sharing with the two adjacent ZrQ_6 octahedra forming a column extending in the *a*-axis direction.

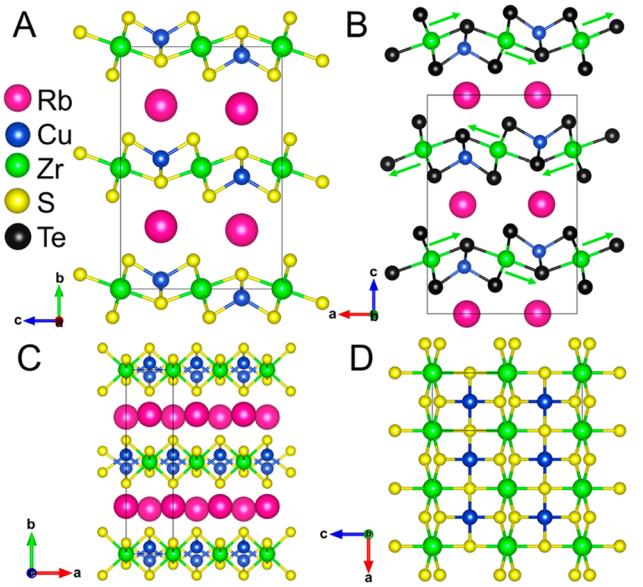

Figure 1. Crystal structure of (A) $RbCuZrS_3$ along the *a*-axis direction and (B) $RbCuZrTe_3$ which exhibits polyhedral distortions. The green arrows show the Zr atoms' direction of off-center in each layer. (C) $RbCuZrS_3$ along the *c* direction and (D) $RbCuZrS_3$ along the *b* direction.

The CuQ_4 tetrahedra are similarly edge-sharing with four adjacent ZrQ_6 octahedra extending in the *c* direction but are corner-sharing with the two adjoining CuQ_4 to form a column that extends along the *a*-axis direction as seen in Figure 1.

The CuQ_4 tetrahedra in this structure are relatively undistorted and exhibit a narrow range of bond lengths that is typical for the respective chalcogen. The ranges of Cu−S bond lengths in $RbCuZrS_3$ are 2.294(3)−2.341(3) Å and in $CsCuZrS_3$ are 2.304(8)−2.332(8) Å. For $RbCuZrSe_3$ the Cu−Se bond lengths range from 2.4101(7) to 2.4476(7) Å. The ZrQ_6 octahedra also do not show distortions and exhibit a narrow range of bond lengths for the respective chalcogen. The ranges of Zr−S bond lengths in $RbCuZrS_3$ and $CsCuZrS_3$ are 2.5910(17)−2.5990(11) Å and 2.591(6)−2.596(4) Å, respectively. For $RbCuZrSe_3$ the range of Zr−Se bond lengths is 2.7120(5)−2.7173(5) Å. The local coordination environment with bond lengths for $RbCuZrS_3$ is shown in Figure 2A,D.

$RbCuZrTe_3$ and $CsCuZrTe_3$ crystallize in a distorted version of the $KCuZrSe_3$ structure type[9] with the lower symmetry space group *Pnma* (No. 62) instead of *Cmcm* (No. 63). The lower symmetry for these tellurides results from an ordered off-centering of the Zr atoms that violate C centering. It is critical to distinguish the structure of $RbCuZrTe_3$ and $CsCuZrTe_3$ from the structures exhibited by the isostoichiometric $NaCuZrSe_3$ and $NaCuZrTe_3$[29] which happen to have the same space group *Pnma* but contain a $[CuZrQ_3]^-$ layer with different polyhedral connectivity resulting in distinct structure types. In $NaCuZrSe_3$ and $NaCuZrTe_3$[29] the $[CuZrQ_3]^-$ layer exhibits alternating pairs of CuQ_4 tetrahedra columns and ZrQ_6 octahedra columns (CuQ_4-CuQ_4-ZrQ_6-ZrQ_6). In $RbCuZrTe_3$ and $CsCuZrTe_3$ the columns of polyhedra still alternate but with the sequence (CuQ_4-ZrQ_6-CuQ_4-ZrQ_6) as observed in the $KCuZrSe_3$ structure type.[9] Figure 3 shows what structure type each of the 12 $ACuZrQ_3$ (A = Na, K, Rb, Cs; Q = S, Se, Te) compositions adopts.

https://doi.org/10.1021/acs.chemmater.2c02104
Chem. Mater. 2022, 34, 8389−8402

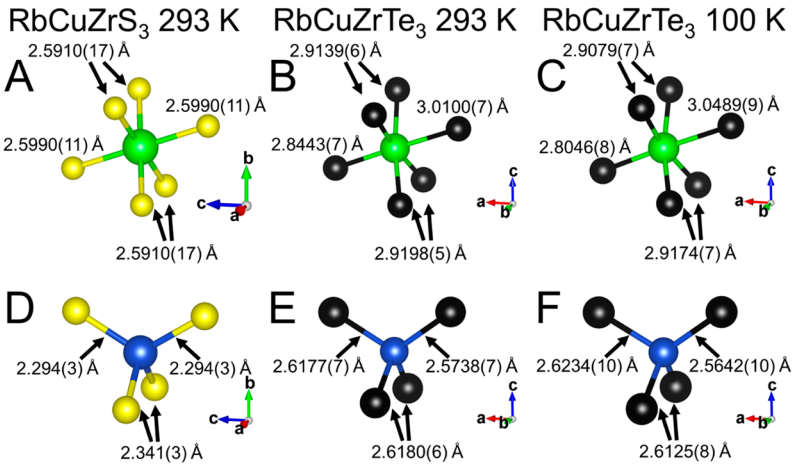

Figure 2. Local coordination environment of the Zr octahedra for (A) $RbCuZrS_3$ at 293 K, (B) $RbCuZrTe_3$ at 293 K, and (C) $RbCuZrTe_3$ at 100 K. The Zr exhibits ordered off-centering in $RbCuZrTe_3$ which increases in magnitude by 47.4% when cooled from 293 to 100 K. (D–F) Local coordination environment of the Cu tetrahedra for the same compounds and temperature.

	Na	K	Rb	Cs
S	*$KCuZrSe_3$* (*Cmcm*)	*$KCuZrSe_3$* (*Cmcm*)	*$KCuZrSe_3$* (*Cmcm*)	*$KCuZrSe_3$* (*Cmcm*)
Se	$NaCuZrSe_3$ (*Pnma*)	*$KCuZrSe_3$* (*Cmcm*)	*$KCuZrSe_3$* (*Cmcm*)	*$KCuZrSe_3$* (*Cmcm*)
Te	$NaCuZrSe_3$ (*Pnma*)	*$KCuZrSe_3$* (*Cmcm*)	Distorted $KCuZrSe_3$ (*Pnma*)	Distorted $KCuZrSe_3$ (*Pnma*)

Figure 3. Compositional map showing what structure type and space group has been reported for $ACuZrQ_3$ where A = Na, K, Rb, Cs and Q = S, Se, Te. Blue boxes are reported to adopt the $KCuZrSe_3$ structure type. Purple boxes are reported to adopt the $NaCuZrSe_3$ structure type. Green boxes are reported to adopt a distorted $KCuZrSe_3$ structure type with Zr off-centering.

For $RbCuZrTe_3$ and $CsCuZrTe_3$ the lower symmetry space group resulted in models such that the crystallographic directions did not end up identical with those crystallizing in the *Cmcm* $KCuZrSe_3$ structure type[9] but can be mapped for ease of comparison. The stacking direction and longest axis in $KCuZrSe_3$ is the *b* direction, while for $RbCuZrTe_3$ and $CsCuZrTe_3$ it is the *c* direction. The shortest axis and the direction that the metal polyhedra alternate along is the *c* direction in $KCuZrSe_3$ while for $RbCuZrTe_3$ and $CsCuZrTe_3$ that is the *a*-axis direction. This leaves the *a*-axis direction in $KCuZrSe_3$ which corresponds to the *b*-axis direction for $RbCuZrTe_3$ and $CsCuZrTe_3$. The zirconium off-centering in $RbCuZrTe_3$ and $CsCuZrTe_3$ expresses as every Zr atom in a given $[CuZrQ_3]^-$ layer distorting in the same crystallographic direction as each other. The direction of off-centering alternates between the positive *a* and the negative *a* directions for every adjacent $[CuZrQ_3]^-$ layer as indicated with green arrows in Figure 1B. The local coordination environments for ZrQ_6 and CuQ_4 for $RbCuZrS_3$ at 293 K and for $RbCuZrTe_3$ at both 293 and 100 K are shown in Figure 2. The zirconium off-centering results in one short and one long axial Zr–Te bond and four nearly equal equatorial Zr–Te bonds. It is noteworthy that the two different space groups *Cmcm* and *Pnma* have different extinction conditions due to the difference in centering conditions which enables confidence in the proper assignment of space group for these materials. Unsurprisingly, the observed reflection intensities in the single crystal data of the tellurides that violate the C centering conditions are low as these reflections would have been systematically absent if the Zr atom were not off-centering in its octahedral environment.

Crystallographic data were collected at 293 K for $RbCuZrTe_3$ and $CsCuZrTe_3$ and at 100 K for $RbCuZrTe_3$. In all three data sets the copper tetrahedra show small distortions with 293 K Cu–Te bond lengths in $CsCuZrTe_3$ ranging from 2.577(3) to 2.6190(17) Å for $CsCuZrTe_3$ while in $RbCuZrTe_3$ ranging from 2.5738(7) to 2.6177(7) Å at 293 K and ranging from 2.5642(10) to 2.6234(10) Å at 100 K. The distortion is smaller in $CsCuZrTe_3$ where the difference between the shortest and longest Cu–Te bonds is 0.042(5) Å. By comparison, $RbCuZrTe_3$ has a difference of 0.0439(14) Å at 293 K, which increases upon cooling by 34.8% to a difference of 0.0592(20) Å at 100 K.

The $ZrTe_6$ octahedral distortions observed in all three data sets are larger than the copper distortions. The Zr–Te bond lengths in $CsCuZrTe_3$ range from 2.8571(15) to 2.9883(15) Å. The Zr–Te bond lengths in $RbCuZrTe_3$ range from of 2.8443(7) to 3.0100(7) Å at 293 K and from 2.8046(8) to 3.0489(9) Å at 100 K. The distortion of the Zr coordination is smaller in $CsCuZrTe_3$ with a difference between the short and long Zr–Te bond lengths of 0.1312(30) Å. By comparison, $RbCuZrTe_3$ has a difference of 0.1657(14) Å at 293 K and increases by 47.4% upon cooling to a range of 0.2443(17) Å at 100 K. This results in Zr off-centering of 0.0656(30) Å in $CsCuZrTe_3$ at 293 K, 0.0829(14) Å in $RbCuZrTe_3$ at 293 K, and 0.1222(17) Å in $RbCuZrTe_3$ at 100 K.

The occurrence of Zr distortions in $[CuZrQ_3]^-$ layers in $ACuZrQ_3$ (A = Rb, Cs; Q = S, Se, Te) materials is clearly influenced by the nature of both the chalcogenide and alkali metal. Distortions occur only for larger chalcogenides. One possibility is that the ZrQ_6 octahedral cage that the Zr^{4+} sits in is an adequate size for the smaller chalcogenides. Once the chalcogen is sufficiently large, the octahedral cage is too big for the Zr^{4+} to occupy the center. The Zr^{4+} then must distort toward one side of the octahedral cage to address this instability. The off-centering distortion results in additional orbital mixing with the now closer anions, resulting in stronger bonds, which is greater than the lengthening/weakening of

https://doi.org/10.1021/acs.chemmater.2c02104
Chem. Mater. 2022, 34, 8389–8402

corresponding bonds on the opposite side, thereby stabilizing the off-centering. Therefore, this is a second-order Jahn−Teller distortion and consistent with the increased bonding interactions observed below the Fermi level for $RbCuZrTe_3$ and $CsCuZrTe_3$ shown in the COHP curves discussed later. This is also consistent with how second-order Jahn−Teller distortions stabilize distortions. Considering the influence of the alkali metal, we see that the magnitude of the off-centering is more prominent in the case of the smaller alkali metal Rb than for Cs at 293 K. Substituting to a smaller alkali metal atom can be thought of as increasing the chemical pressure squeezing the layers closer together. With the larger amount of chemical pressure in $RbCuZrTe_3$, the $[CuZrQ_3]^-$ slab gets squished by the electrostatic repulsion of the adjacent slabs. This secondary effect results in the ZrQ_6 octahedra distorting by getting squished along the stacking direction and the Zr^{4+} atoms shifting to one side in the plane of the $[CuZrQ_3]^-$ slab to alleviate this pressure. This is further supported by the observation that cooling $RbCuZrTe_3$ from 293 to 100 K simultaneously results in thermal contraction of the unit cell bringing the slabs closer together, combined with the magnitude of the zirconium off-centering increasing by 47.4% from 0.0829(14) to 0.1222(17) Å. When this driving force is further increased in the case of the sodium analogue $NaCuZrTe_3$, the $[CuZrQ_3]^-$ slab that forms has ultimately rearranged to the alternating column sequence of (Zr−Zr−Cu−Cu) as described above while still exhibiting some Zr distortions.

β-$CsCuS_4$ was identified as a side product when making $CsCuZrS_3$ and is found to crystallize in the β-$KCuS_4$ structure type[30] with the space group $P\bar{1}$ shown in Figure 4A,B. The

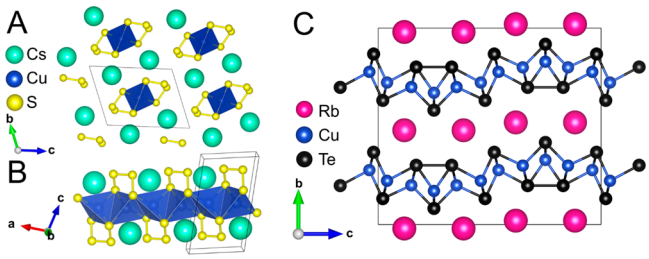

Figure 4. Crystal structure of β-$CsCuS_4$ (A) looking down the *a*-axis direction parallel to the $[CuS_4]^-$ polymeric chains and (B) looking along the *b* direction showing the edge-sharing Cu tetrahedra. (C) Crystal structure of $Rb_2Cu_5Te_5$ looking down the *a*-axis direction with the ditelluride Te_2 bond drawn.

structure has Cs^+ ions and one-dimensional $[CuS_4]^-$ chains of edge-sharing copper tetrahedra. The structure has S_4^{2-} polysulfide units and is similar to $CsCuS_6$ which has longer S_6^{2-} polysulfide units. The difference between β-$CsCuS_4$ from α-$CsCuS_4$, isostructural to α-$KCuS_4$,[30] is that the $[CuS_4]^-$ chains exhibit corner-sharing connectivity.

$Rb_2Cu_5Te_5$ was also identified as a side product when making $RbCuZrTe_3$ and is isostructural to $K_2Cu_5Te_5$[31] with the space group *Cmcm*. The structure, shown in Figure 4C, features $[Cu_5Te_5]^{2-}$ layers with charge balancing Rb^+ cations between the layers. All the Cu atoms are tetrahedral, and there is a ditelluride Te_2^{2-} unit in the $[Cu_5Te_5]^{2-}$ layer with a long Te−Te bond of 2.9720(10) Å. The mixed valency and bonding nature in this structure type has been discussed in detail by Park et al. for $K_2Cu_5Te_5$.[31] The chemical composition for all materials reported here was confirmed by using energy dispersive spectroscopy (EDS) in a scanning electron microscope (SEM) shown in Figures S5−S8.

Differential Thermal Analysis and Variable Temperature PXRD. The thermal behavior of the five $ACuZrQ_3$ materials was investigated by using differential thermal analysis (DTA) data combined with powder X-ray diffraction (PXRD) before and after the DTA. This is shown in Figure 5 for $CsCuZrS_3$ and $CsCuZrTe_3$ and in Figures S9−S13 for the $RbCuZrQ_3$ (Q = S, Se, Te). $CsCuZrS_3$ in Figure 5A shows multiple reproducible thermal events during both heating and cooling cycles, with the diffraction pattern practically unchanged after the DTA, as seen in Figure 5B. During both heating cycles, there are endothermic events that occur at 455 and 580 °C, and during both cooling cycles there are exothermic events that occur at 905, 616, and 464 °C. Moreover, there is an anomalous broad exothermic event observed during only the first heating cycle that starts 750 °C.

To probe the nature of these thermal events, we performed variable temperature PXRD on already synthesized $CsCuZrS_3$ from 20 to 930 °C as shown in Figure 6. Upon heating at 275 °C, a set of new Bragg reflections can be seen coming in simultaneously, which persist until 575 °C when they all disappear simultaneously. The appearance of these new reflections is coupled with a decrease in intensity for the Bragg reflections corresponding to $CsCuZrS_3$. The new Bragg reflections that come in at 275 °C and disappear at 575 °C are assigned to the phase $CsCuS_6$. The last heating scan where the $CsCuZrS_3$ reflections are observed is at 900 °C, and they all disappeared by the next scan at 910 °C, which persists to the maximum temperature of 930 °C. Upon cooling, the $CsCuZrS_3$ reflections reappear in the 900 °C scan and continue to grow in intensity and experience thermal contraction during the rest of the cooling. Additionally, we see the reflections for $CsCuS_6$ reappear on cooling at 525 °C, persisting to room temperature through the end of the experiment. Some residual red material was observed visually at the end of the experiment, consistent with the color of $CsCuS_6$. On the basis of this experiment, we assign the melting point of 910 °C and the crystallization point for $CsCuZrS_3$ as 905 °C. Additionally, $CsCuZrS_3$ seems to undergo partial decomposition during heating, where the additional thermal events observed in the DTA are explained by the behavior of the secondary phase $CsCuS_6$. The lack of $CsCuS_6$ at the end of the DTA experiment observable in the PXRD pattern is likely due to a smaller proportion of the material having decomposed because of the much faster cooling rate in the DTA experiment. This observation of $CsCuS_6$ as the decomposition product instead of β-$CsCuS_4$ was surprising as only β-$CsCuS_4$ was observed as a side product from the initial synthesis. This indicates that β-$CsCuS_4$ is not a decomposition product but a side product likely involved in the reaction pathway that formed $CsCuZrS_3$ that did not fully react.

$RbCuZrS_3$ did not show any reproducible thermal events in the DTA in Figure S9 but does produce trace orange/red material found on the bottom of the post-DTA material as shown in Figure S9C. Additionally, a minor impurity Bragg reflection found at 9.3° 2θ, which is located at a lower Bragg angle than the first $RbCuZrS_3$ reflection at 12.1° 2θ, is observed in the post-DTA PXRD powder pattern. This indicates that $RbCuZrS_3$ also undergoes partial decomposition either during heating or cooling, resulting in a phase that is likely a $RbCuS_4$ or $RbCuS_6$ phase.

https://doi.org/10.1021/acs.chemmater.2c02104
Chem. Mater. 2022, 34, 8389−8402

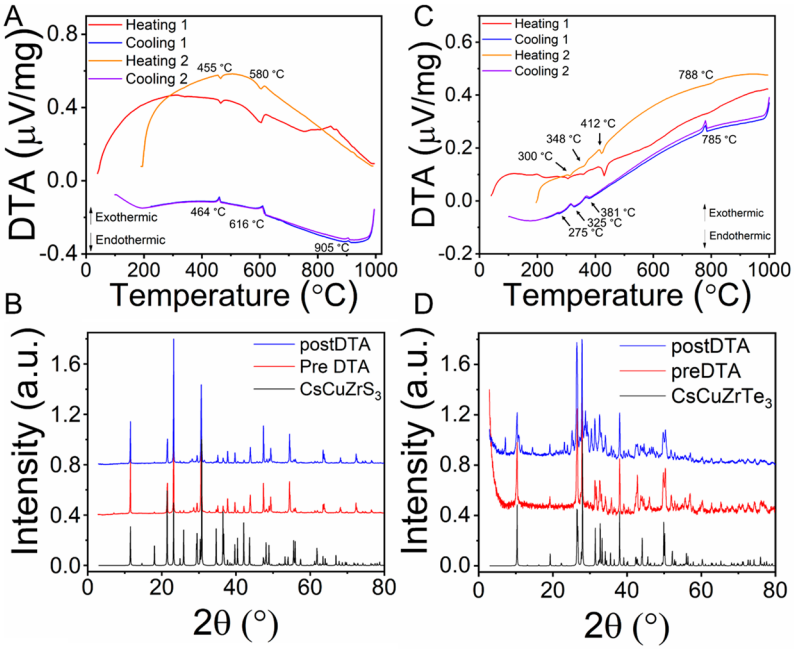

Figure 5. (A) Differential thermal analysis (DTA) with a ramp rate of 10 °C/min for $CsCuZrS_3$ with endothermic events during heating at 455 and 580 °C and exothermic events during cooling at 905, 616, and 464 °C. (B) PXRD before and after DTA indicates that the material is recovered after DTA. (C) DTA of $CsCuZrTe_3$ shows reproducible endothermic events during heating at 300, 348, 412, and weakly at 788 °C and exothermic events upon cooling at 785, 381, 325, and 275 °C. (D) PXRD before and after DTA shows that partial decomposition during DTA has occurred in an unidentified phase.

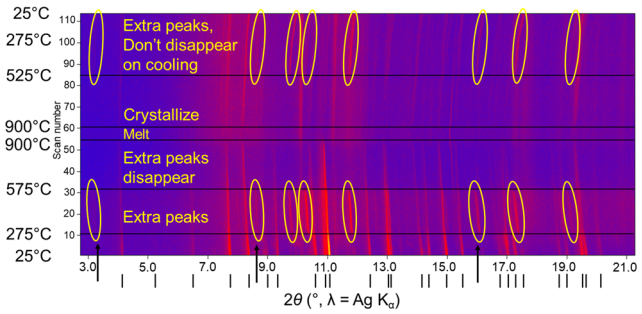

Figure 6. Variable temperature PXRD using Ag Kα radiation with RT reflections for $CsCuZrS_3$ indicated with black tick marks. Upon reaching 275 °C a series of new reflections come in simultaneously circled in black, which we match to $CsCuS_6$ which then disappears at 575 °C. Subsequently $CsCuZrS_3$ melts by 910 °C until the maximum temperature of 930 °C. Upon cooling, $CsCuZrS_3$ is observed recrystallizing at 900 °C. The extra Bragg reflections are from $CsCuS_6$ reappearing during cooling at 525 °C. An unidentified high symmetry minor phase slowly gains intensity throughout the experiment.

The DTA of $RbCuZrSe_3$ shown in Figure S10 shows an endothermic event at 850 °C on the first heating cycle but then on the second heating cycle exhibits a very broad exothermic event from 690 to 907 °C. It did not reveal any thermal events on cooling. The PXRD before and after the DTA analysis shows that the material is unchanged after the DTA, and the images shown in Figure S10C show that the ground powder loaded into the ampoule has formed crystals. This suggests the material was annealed and formed crystals without melting as there is no observable exothermic event to assign as a crystallization point from having reached a melting point. The cause of the broad exothermic feature during the second heating cycle is unknown.

The DTA of $RbCuZrTe_3$ shows reproducible endothermic events during both heating cycles at 340 °C and a very weak event at 893 °C and shows exothermic events upon cooling at 878 and 330 °C (Figure S11A). The PXRD shown in Figure S11B shows that the pattern is mostly unchanged with a small additional shoulder on the higher Bragg angle side of the first reflection. The material looks like a solidified ingot at the end of the process. On the basis of this, $RbCuZrTe_3$ seems to melt congruently with a melting point of 893 °C. The origin of the 340 °C/330 °C event in the heating/cooling cycles may be due to a trace impurity or partial decomposition event that requires additional variable temperature PXRD experiments to study further.

The DTA of $CsCuZrTe_3$ has additional thermal events than $RbCuZrTe_3$ as shown in Figure 5C. Upon heating, we observed reproducible endothermic thermal events during both heating cycles at 300, 348, and 412 °C and an extremely weak event at 788 °C. Upon cooling, there are reproducible exothermic thermal events during both cooling cycles at 785, 381, 325, and 275 °C. The 785 °C events are assigned as the melting and crystallization events. The nature of the low-temperature events, however, is unclear and requires variable temperature PXRD studies to probe. The PXRD of the post DTA sample shown in Figure 5D indicates that the material has partially decomposed with additional diffraction peaks present, which could not be identified. They could be from a Cs/Cu/Te phase similar to the new $Rb_2Cu_5Te_5$ compound reported here.

Optical and Electronic Properties. The optical absorption properties of $RbCuZrQ_3$ (Q = S, Se, Te), $CsCuZrS_3$, and $CsCuZrTe_3$ were investigated by using UV−vis diffuse reflectance spectroscopy and photoemission yield spectroscopy in air (PYSA) measurements shown in Figure 7. The UV−vis data were used to determine the bandgap by extrapolating the

https://doi.org/10.1021/acs.chemmater.2c02104
Chem. Mater. 2022, 34, 8389−8402

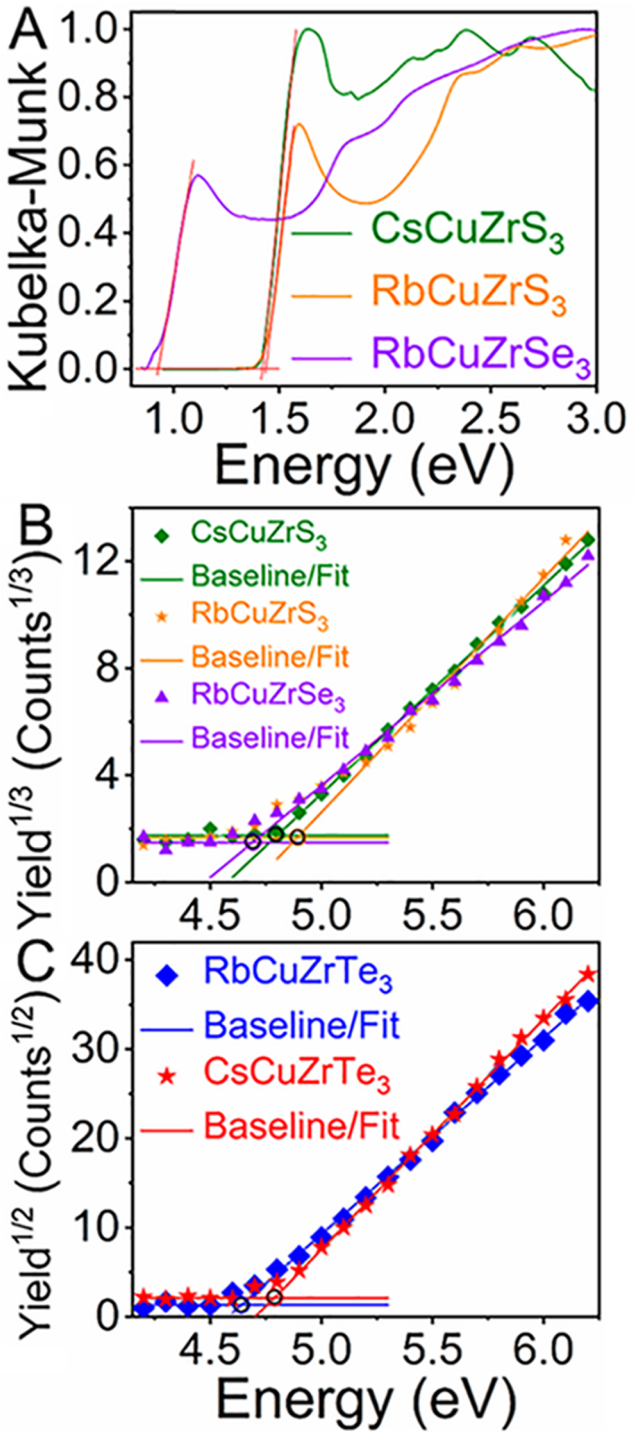

Figure 7. (A) Optical absorption spectra showing bandgaps of 1.42(5) eV $CsCuZrS_3$ (green), 1.44(5) eV for $RbCuZrS_3$ (orange), and 0.95(5) eV $RbCuZrSe_3$ (purple). (B) Photoemission yield spectra in air (PYSA) showing work functions of 4.80(5) eV $CsCuZrS_3$, 4.89(5) eV for $RbCuZrS_3$, and 4.67(5) eV $RbCuZrSe_3$. (C) PYSA data showing work functions of 4.64(5) eV for $RbCuZrTe_3$ (blue) and 4.79(5) eV for $CsCuZrTe_3$ (red).

linear onset of the absorption edges. For $RbCuZrS_3$ the bandgap was found to be 1.44(5) eV (861 nm), while for $CsCuZrS_3$ it was 1.42(5) eV (873 nm). These values are within the error of the measurement of each other, which is reasonable since substitution of alkali metal would not be expected to substantively change the energy of the orbitals that comprise the valence or conduction band edges. For $RbCuZrSe_3$ the bandgap was found to be 0.95(5) eV (1305 nm). This value is reasonable compared to the sulfide analogue since isostructural substitution for a heavier chalcogen is expected to narrow the bandgap. This is because the smaller electronegativity difference between the metals and the Se combined with the more extended Se orbitals compared with those of S have greater orbital overlap resulting in broader electronic bands that narrow the bandgap. UV−vis diffuse reflectance and IR spectroscopy of $CsCuZrTe_3$ did not indicate an optical bandgap between 0.09 eV (13800 nm) and 3.50 eV (354 nm).

The PYSA measurements were performed to find the work functions that were determined by extrapolating the linear onset of the data.[32,33] For semiconductors, the work function is equal to the energy of the valence band maximum (VBM) with respect to the energy of a free electron. Considering the bandgap in combination with the work function allows for determining the energy level of the conduction band minimum (CBM) with respect to the energy of a free electron. For $RbCuZrS_3$ the work function was found to be 4.89(5) eV while for $CsCuZrS_3$ it is 4.80(5) eV. These results, taken together with the bandgap values for $RbCuZrS_3$, yield a VBM of 4.89(5) eV and a CBM of 3.45(7) eV while for $CsCuZrS_3$ yield a VBM of 4.80(5) eV and a CBM of 3.38(7) eV. These values are within error of each other, which is reasonable for the same reason described for the bandgaps. For $RbCuZrSe_3$ the work function was found to be 4.67(5) eV. This value taken together with the bandgap results in a VBM of 4.67(5) eV and a CBM of 3.72(7) eV. The shallower VBM and deeper CBM of $RbCuZrSe_3$ compared with $RbCuZrS_3$ are consistent with the explanation provided for the narrower bandgap. For $RbCuZrTe_3$ and $CsCuZrTe_3$ the work functions were 4.64(5) and 4.79(5) eV, respectively.

Electronic Structure Calculations. The electronic band structure, the partial density of states (PDOS), and crystal orbital Hamilton population (COHP) plots for for $RbCuZrS_3$ and $RbCuZrTe_3$ are shown in Figure 8. For $RbCuZrSe_3$, $CsCuZrS_3$, and $CsCuZrTe_3$ they are shown in Figures S15, S16, and S17, respectively. Considering $RbCuZrS_3$, $RbCuZrSe_3$, and $CsCuZrS_3$ first, their electronic band structures reveal direct bandgaps at the Γ point calculated to be 0.533, 0.122, and 0.57 eV, respectively. These values are underestimated compared to the experimentally observed bandgaps, a well-known DFT limitation.[34]

The electronic structure reveals linearly dispersive bands at the VBM along the Γ−X and Γ−Z directions, while the VBM is almost dispersionless along the Γ−Y direction for all three materials. Considering the representative $RbCuZrS_3$, the calculated hole effective masses are −0.316 m_0 along Γ−X and −0.706 m_0 along Γ−Z compared with −5.345 m_0 along Γ−Y, where m_0 is the free electron mass. The dispersion in the CBM is consistent between $RbCuZrS_3$ and $RbCuZrSe_3$ but differs from $CsCuZrS_3$. All three materials have a linearly dispersive band along the Γ−X direction. $RbCuZrS_3$ and $RbCuZrSe_3$ are least dispersive along the Γ−Z direction with the Γ−Y direction in the middle while for $CsCuZrS_3$ the Γ−Y direction is the least dispersive and the Γ−Z direction is in the middle.

For $RbCuZrS_3$, the calculated electron effective masses are 0.407 m_0 along Γ−X and 3.552 m_0 along Γ−Z compared with 1.550 m_0 for the Γ−Y direction. For $CsCuZrS_3$ the calculated electron effective masses are 0.387 m_0 along Γ−X, 1.949 m_0

https://doi.org/10.1021/acs.chemmater.2c02104
Chem. Mater. 2022, 34, 8389−8402

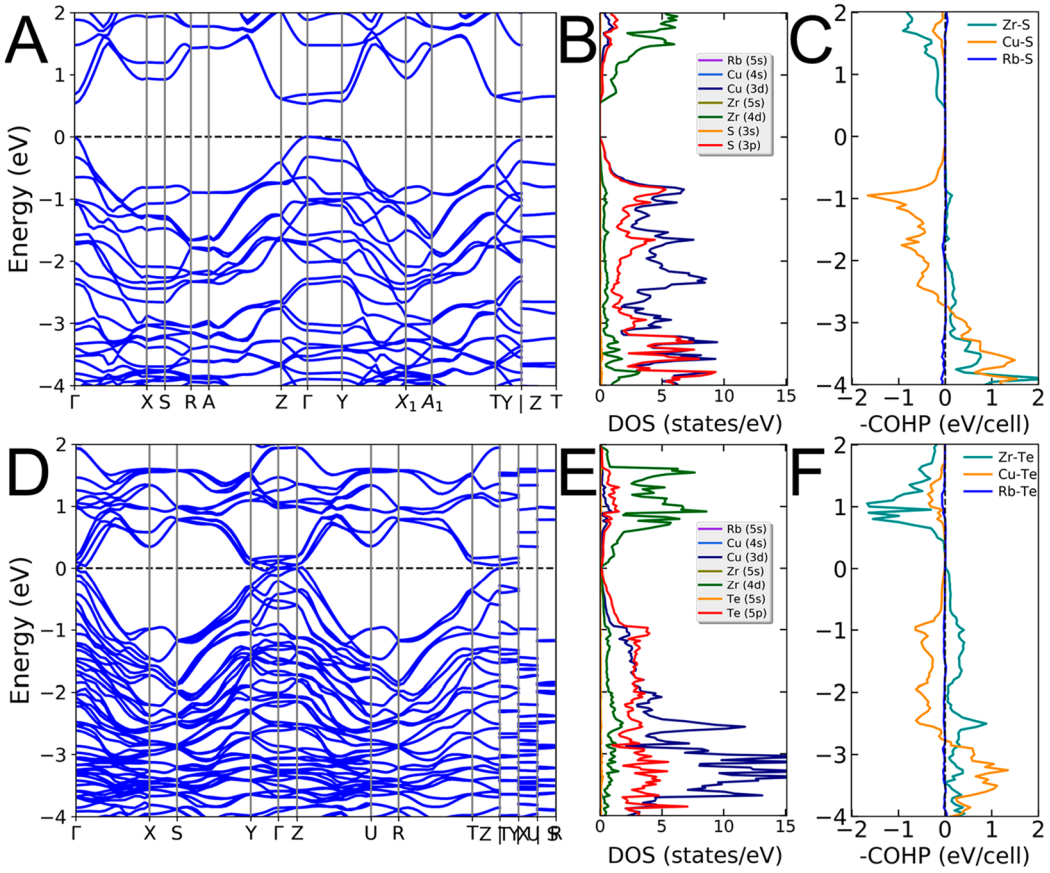

Figure 8. (A) DFT-calculated electronic structure, (B) partial density of states (DOS), and (C) crystal orbital Hamilton population (COHP) plots for $RbCuZrS_3$. Analogous plots for $RbCuZrTe_3$ are shown in (D−F). The negative and positive −COHP values indicate antibonding and bonding interactions, respectively.

along Γ−*Z*, and 4.245 m_0 along Γ−*Y*. The effective masses for both electrons and holes for all three materials are presented in Table 3. The relatively low carrier effective masses in the VBM and CBM along the Γ−*X* direction, which corresponds to the *a* crystallographic direction that the columns of metal polyhedra propagate along, are conducive for high carrier mobilities. On the other hand, the much heavier masses along the Γ−*Y* and Γ−Z directions, which are the *b* and *c* crystallographic directions, respectively, should result in low mobilities in these directions.

Table 3. Calculated Effective Masses in Units of m_0 for Electrons at the Conduction Band Minimum and Holes at the Valence Band Maximum

direction	$RbCuZrS_3$	$RbCuZrSe_3$	$CsCuZrS_3$
	electrons		
Γ → X	0.407	0.385	0.387
Γ → Y	1.550	0.901	4.245
Γ → Z	3.552	2.330	1.949
	holes		
Γ → X	−0.316	−0.287	−0.323
Γ → Y	−5.345	−2.881	−5.091
Γ → Z	−0.706	−0.405	−0.682

To understand the orbital contributions to the band structure, we have calculated the PDOS (Figure 8B), which shows that valence bands primarily consist of the 3p orbitals of S that strongly hybridize with 3d orbitals of Cu. In contrast, the conduction band mainly results from the empty 4d orbitals of Zr. To gain further insights into the nature of the chemical bonding, we performed COHP analysis[25,26] which partitions the energy of the band structure into pairs of orbital or atomic interactions. The COHP analysis reveals that p−d interactions between S and Cu below the Fermi level are antibonding in nature and dominate the valence band down to −2.5 eV. These filled antibonding states weaken the bond strength in the material and lead to soft phonon frequencies—a requisite for low lattice thermal conductivity.

To this end, we calculated the phonon dispersions shown in Figure 9A for $RbCuZrS_3$ and in Figures S18 and S19 for $RbCuZrSe_3$ and $CsCuZrS_3$, respectively. All the phonon modes for these materials are positive, signifying their dynamical stability. Interestingly, the phonon dispersion for these materials exhibits nearly dispersionless low-energy phonon branches along the entire Brillouin zone (except near the Γ-point). The analysis of atom-resolved phonon density (Figure 9B) of states shows that the dispersionless phonon branches mainly arise from the alkali metal vibrational modes, which give rise to two sharp peaks (at 50 and 74 cm^{-1}) for $RbCuZrS_3$ and for $CsCuZrS_3$ (at 38 and 62 cm^{-1}). These phonon branches signify the rattling-like vibrations of the Rb and Cs atoms in layers of the crystal structure. Because rattler cations are shown to scatter phonons effectively, these materials are expected to exhibit low lattice thermal conductivities.

https://doi.org/10.1021/acs.chemmater.2c02104
Chem. Mater. 2022, 34, 8389−8402

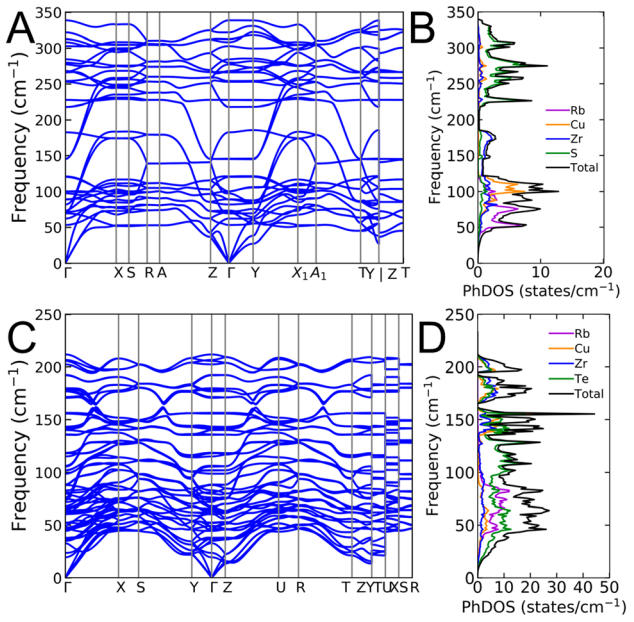

Figure 9. (A) DFT-calculated phonon dispersion and (B) atom-resolved phonon density of states for $RbCuZrS_3$. Analogous plots for $RbCuZrTe_3$ are shown in (C) and (D).

The calculated electronic structures for $RbCuZrTe_3$ and $CsCuZrTe_3$ differ from the sulfide and selenide analogues in that they predict these tellurides are metals instead of semiconductors as shown in Figures 8D and S20, respectively. This prediction is supported by the lack of an observable optical bandgap and the fact that measured temperature-dependent conductivity for the potassium analogue $KCuZrTe_3$ was found to be a metal.[9] The PDOS shown in Figure 8E and the COHP plots in Figure 8F show that below the Fermi level mainly consist of antibonding p−d hybridized states between Cu and Te and above the Fermi level is primarily composed of Zr 4d states. Noteworthy, however, is the presence of substantive amounts of bonding interactions between empty Zr 4d states and the filled Te 5p between the Fermi level and −2 eV below the Fermi level shown in Figure 8F for $RbCuZrTe_3$ and in Figure S17 for $CsCuZrTe_3$. The degree of bonding interactions between Zr 4d states and Te 5p is notably greater than what is seen for the sulfide (Figures 8C and S16C) and selenide (Figure S15C) analogues in the top 2 eV of the valence band. Additionally, the amount of bonding interactions in $RbCuZrTe_3$ is much greater than what is observed in the band structure of $RbCuZrTe_3$, taking a theoretical $KCuZrSe_3$ structure type with Zr centered in its octahedral environment with the *Cmcm* space group with undistorted Zr environments shown in Figure S24C. Interestingly, the phonon dispersion for $RbCuZrTe_3$ taking the theoretical $KCuZrSe_3$ structure type with the *Cmcm* space group exhibits negative phonon modes shown in Figure S25 not observed for the experimental structure phonon dispersion shown in Figure 9C,D. The most negative phonon mode for the theoretical $RbCuZrTe_3$ structure at the Γ-point corresponds to a vibration mode that includes Zr moving off the center of the Zr octahedra.

Taking all of the above together, we can surmise that the long-range ordered off-centering of the Zr atoms in $RbCuZrTe_3$ and $CsCuZrTe_3$ is the result of the Zr atoms moving off-centering toward an axial Te in the octahedra Zr environment. This increases the orbital overlap and bonding interaction of Zr 4d states with the closer axial Te 5p state, which manifests in the COHP plot and provides the energetic driving force. As mentioned above, this type of distortion can be understood as a second-order Jahn−Teller distortion.[35−39]

Resistivity and Thermoelectric Properties. The room temperature electrical resistivity was measured by using single crystals of $CsCuZrS_3$ and $RbCuZrSe_3$ as shown in Figures S22 and S23, respectively. Both materials exhibited ohmic behavior with no hysteresis for two cycles when enclosed in a light-tight box and upon exposure to ambient room light. $CsCuZrS_3$ and $RbCuZrSe_3$ samples were both fairly conductive with $CsCuZrS_3$ having a resistivity of 1×10^2 Ω·cm while $RbCuZrSe_3$ has a resistivity of 1×10^1 Ω·cm, suggesting they are extrinsically doped. The temperature-dependent electrical conductivity (σ), Seebeck (S), and thermal conductivity (κ) were measured for $RbCuZrTe_3$ and are shown in Figure 10. The sample shows a decent room temperature electrical conductivity of about 80 S cm^{-1}, decreasing with rising temperature. The electrical conductivity behavior indicates that the sample is a metal which is consistent with the calculated electronic band structure

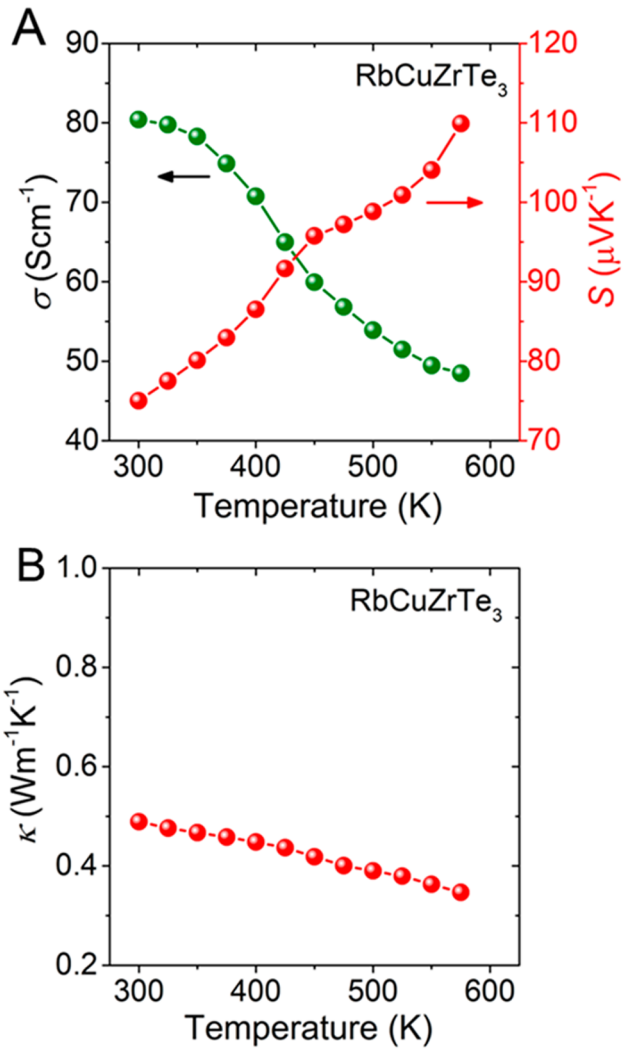

Figure 10. Thermoelectric property measurements of $RbCuZrTe_3$ showing (A) electrical conductivity and Seebeck coefficient and (B) thermal conductivity below 0.50 W m^{-1} K^{-1} at room temperature.

https://doi.org/10.1021/acs.chemmater.2c02104
Chem. Mater. 2022, 34, 8389−8402

prediction that the material is a metal and the lack of an observable optical bandgap. The positive Seebeck coefficient indicates the sample is a p-type material. The temperature-dependent Seebeck coefficient follows the usual inverse relationship with respect to the temperature dependence of electrical conductivity, which increases from 75 μV K^{-1} at room temperature to 115 μV K^{-1} at 593 K as shown in Figure 10A.

The temperature-dependent total thermal conductivity for $RbCuZrTe_3$ is shown in Figure 10B. The total thermal conductivity is extremely low at 0.49 W m^{-1} K^{-1} at room temperature and drops to 0.34 W m^{-1} K^{-1} at 575 K. The lattice thermal conductivity, which is 0.44 W m^{-1} K^{-1} at room temperature and decreases to 0.29 W m^{-1} K^{-1} at 575 K, is shown in Figure S27E. This ultralow thermal conductivity should be attributed to the strong phonon−phonon scattering, caused by the rattling-like vibrations of the Rb and the Zr distortion. This ultralow thermal conductivity is consistent with the recent thermal conductivity predictions for this class of materials by Pal et al.[8] $CsCuZrS_3$ was predicted at 300 K to have in-plane thermal conductivity of 1.0 W m^{-1} K^{-1} and out-of-plane thermal conductivity of 3.0 W m^{-1} K^{-1}, and we expect the Te analogue to have lower thermal conductivity than the sulfide.[8] This low thermal conductivity suggests that materials with this structure type have potential as thermoelectric materials. The selection of a composition with a narrow bandgap such as a potential Se−Te solid solution combined with doping to optimize the carrier concentration has promise for a material that retains the desirable very low thermal conductivity make it promising future thermoelectric investigations.[40]

Heat Capacity. The heat capacity of $RbCuZrTe_3$ and $CsCuZrTe_3$ was measured between 3.8 and 275 K to investigate for evidence of a low-temperature phase transition as shown in Figure S28. Both materials did not show any discontinuities over this temperature range, indicating that there are no first-order phase transitions. At sufficiently low temperatures the heat capacity can be expressed as $C_p = \gamma T + \beta T^3$, where γ parametrizes the electronic contributions to the specific heat and β determines the lattice contribution.[41] In the low-temperature region the relationship of C_p/T vs T^2 should become linear where β is approximated as the slope and γ is approximated as the y-intercept.[42] The Debye temperature θ_D is the characteristic temperature of the largest lattice vibrations of a material which is approximated from β as described in the Supporting Information. For $CsCuZrTe_3$ the relationship of C_p/T vs T^2 is linear for T between 3.8 and 4.4 K while for $RbCuZrTe_3$ it is linear for T between 3.8 and 4.1 K. For $CsCuZrTe_3$, these parameters were determined to be $\theta_D \approx$ 170(5) K, $\gamma \approx$ 84.6(8) mJ mol^{-1} K^{-2}, and $\beta \approx$ 2.47(37) mJ mol^{-1} K^{-4}. For $RbCuZrTe_3$, $\theta_D \approx$ 150(5) K, $\gamma \approx$ 9.24(98) mJ mol^{-1} K^{-2}, and $\beta \approx$ 3.67(62) mJ mol^{-1} K^{-4}. The γ value is proportional to the density of states at the Fermi surface so the positive values for $RbCuZrTe_3$ and $CsCuZrTe_3$ are additional evidence of the metallic nature of the materials. The γ values are of a similar order of magnitude to each other as well as other metallic materials such as Al[43] which has a $\gamma \approx$ 1.35 mJ mol^{-1} K^{-2} or $YbSb_2$[44] which has a $\gamma \approx$ 3.18 mJ mol^{-1} K^{-2}. The θ_D values for $RbCuZrTe_3$ and $CsCuZrTe_3$ are somewhat lower than the reported values for other low thermal conductivity thermoelectric materials such $NaSn_5SbTe_7$[45] with a $\theta_D \approx$ 164 K and BiAgOSe[46] with a $\theta_D \approx$ 191 K and are also lower than both $YbSb_2$[44] ($\theta_D \approx$ 186 K) and Al[43] ($\theta_D \approx$ 427.7 K). Future measurements to temperatures below 3.8 K which we were unable to obtain due to instrumental limitations at this time would allow for a larger linear region enabling a more accurate determination of these values.

CONCLUDING REMARKS

$RbCuZrS_3$, $RbCuZrSe_3$, and $CsCuZrS_3$ crystallize in the $KCuZrSe_3$ structure type with the space group *Cmcm* while $RbCuZrTe_3$ and $CsCuZrTe_3$ crystallize in the lower symmetry space group *Pnma* due to second-order Jahn−Teller distortion of the d^0 Zr in an ordered off-centering. The distortion is larger for the Rb analogue than the Cs analogue and increases for $RbCuZrTe_3$ upon cooling. DFT calculations predict direct gap semiconductors for the sulfide and selenide compositions, while $ACuZrTe_3$ are correctly predicted to be metals. The bandgaps and work functions are 1.44(5) eV and 4.89(5) eV for $RbCuZrS_3$ and 0.95(5) eV and 4.67(5) eV for $RbCuZrSe_3$, while no optical bandgap was observed for $RbCuZrTe_3$ with a work function of 4.64(5) eV. Variable temperature conductivity of $RbCuZrTe_3$ found metallic behavior. Heat capacity measurements also suggest $RbCuZrTe_3$ and $CsCuZrTe_3$ to be metals with Debye temperatures of 150 and 170 K, respectively. Phonon dispersion calculations at 0 K find low-lying vibrational modes of the alkali metal ions for all the quaternary phases reported here indicative of rattling behavior. $RbCuZrTe_3$ exhibits very low thermal conductivity below 0.5 W m^{-1} K^{-1} at room temperature.

From the point of view of physical property characteristics, we expect these materials to be similar to the recently reported $A_2Cu_2nLn_4Q_{7+n}$ (A = Cs, Rb; Ln = La−Nd, Sm, Gd−Yb; Q = S, Se) homologous series.[46]

ASSOCIATED CONTENT

Supporting Information

The Supporting Information is available free of charge at https://pubs.acs.org/doi/10.1021/acs.chemmater.2c02104.

Additional experimental details, full crystallographic tables, SEM and EDS, differential thermal analysis, powder X-ray diffraction, electronic band structure with DOS and COHP, phonon dispersion with DOS, thermoelectric properties, resistivity measurements, pictures, heat capacity, and Debye temperature (PDF)

$RbCuZrS_3$ CSD deposit number 2189464 (CIF)

$RbCuZrSe_3$ CSD deposit number 2189465 (CIF)

$RbCuZrTe_3$ CSD deposit number 2189466 (CIF)

$RbCuZrTe_3$ at 100 K CSD deposit number 2189467 (CIF)

$CsCuZrS_3$ CSD deposit number 2189468 (CIF)

$CsCuZrTe_3$ CSD deposit number 2189469 (CIF)

$Rb_2Cu_5Te_5$ CSD deposit number 2189471 (CIF)

β-$CsCuS_4$ CSD deposit number 2189470 (CIF)

AUTHOR INFORMATION

Corresponding Author

Mercouri G. Kanatzidis − *Department of Chemistry, Northwestern University, Evanston, Illinois 60208, United States; Materials Science Division, Argonne National Laboratory, Lemont, Illinois 60439, United States;* orcid.org/0000-0003-2037-4168; Email: m-kanatzidis@northwestern.edu

https://doi.org/10.1021/acs.chemmater.2c02104
Chem. Mater. 2022, 34, 8389−8402

Authors

Craig C. Laing − *Department of Chemistry, Northwestern University, Evanston, Illinois 60208, United States;* orcid.org/0000-0002-0654-4741

Benjamin E. Weiss − *Department of Chemistry, Northwestern University, Evanston, Illinois 60208, United States;* orcid.org/0000-0003-0605-3659

Koushik Pal − *Department of Materials Science and Engineering, Northwestern University, Evanston, Illinois 60208, United States*

Michael A. Quintero − *Department of Chemistry, Northwestern University, Evanston, Illinois 60208, United States;* orcid.org/0000-0002-0709-1676

Hongyao Xie − *Department of Chemistry, Northwestern University, Evanston, Illinois 60208, United States;* orcid.org/0000-0002-2472-3866

Xiuquan Zhou − *Materials Science Division, Argonne National Laboratory, Lemont, Illinois 60439, United States*

Jiahong Shen − *Department of Materials Science and Engineering, Northwestern University, Evanston, Illinois 60208, United States;* orcid.org/0000-0002-1951-2183

Duck Young Chung − *Materials Science Division, Argonne National Laboratory, Lemont, Illinois 60439, United States*

Christopher Wolverton − *Department of Materials Science and Engineering, Northwestern University, Evanston, Illinois 60208, United States;* orcid.org/0000-0003-2248-474X

Complete contact information is available at: https://pubs.acs.org/10.1021/acs.chemmater.2c02104

Notes

The authors declare no competing financial interest.

■ ACKNOWLEDGMENTS

Synthesis and material characterization were supported by the National Science Foundation through grant DMR-2003476. This work used the IMSERC Crystallography facility at Northwestern University, which received support from the Soft and Hybrid Nanotechnology Experimental (SHyNE) Resource (NSF ECCS-2025633) and Northwestern University. The Ag-microsource diffractometer used in this study was funded by the Major Research Instrumentation Program from the National Science Foundation under Award CHE-1920248. This work used the IMSERC Physical Characterization facility at Northwestern University, which has received support from the SHyNE Resource (NSF ECCS-2025633), and Northwestern University. This work used the EPIC facility of Northwestern University's NUANCE Center, which received support from the SHyNE Resource (NSF ECCS-2025633), IIN, and Northwestern University's MRSEC program (NSF DMR-1720139). K.P. and C.W. acknowledge funding from National Institute of Standards and Technology as part of the Center for Hierarchical Materials Design (CHiMaD) under Award 70NANB14H012 by U.S. Department of Commerce. The work in the Materials Science Division of Argonne National Laboratory (low-temperature heat capacity measurements) was supported by the U.S. Department of Energy, Office of Science, Basic Energy Sciences, Materials Sciences and Engineering Division, under Contract DE-AC02-06CH11357.

■ REFERENCES

(1) Guo, Z.; Liu, Z.; Deng, J.; Lin, J.; Zhang, Z.; Han, X.; Sun, F.; Yuan, W. Layered quaternary chalcogenides $KMgCuSe_2$ and $KMgCuTe_2$ with paramagnetic semiconducting behavior. *J. Alloys Compd.* **2021**, *883*, 160820.

(2) Liu, Y.; Li, Y.; Guo, Y.; Sun, Y.; Cao, X.; Ji, M.; You, Z.; An, Y. Mild solvothermal syntheses and characterizations of four quaternary layered sulfides $AAgCdS_2$ (A = K, Rb, Cs) and $Cs_2Cu_2Cd_2S_4$. *J. Alloys Compd.* **2020**, *847*, 156450.

(3) Pomelova, T. A.; Podlipskaya, T. Y.; Kuratieva, N. V.; Cherkov, A. G.; Nebogatikova, N. A.; Ryzhikov, M. R.; Huguenot, A.; Gautier, R.; Naumov, N. G. Synthesis, Crystal Structure, and Liquid Exfoliation of Layered Lanthanide Sulfides KLn_2CuS_6 (Ln = La, Ce, Pr, Nd, Sm). *Inorg. Chem.* **2018**, *57* (21), 13594−13605.

(4) Quintero, M. A.; Hao, S.; Patel, S. V.; Bao, J.-K.; Zhou, X.; Hu, Y.-Y.; Wolverton, C.; Kanatzidis, M. G. Lithium Thiostannate Spinels: Air-Stable Cubic Semiconductors. *Chem. Mater.* **2021**, *33* (6), 2080−2089.

(5) Xiao, Y.; Zhou, S.-H.; Yu, R.; Shen, Y.; Ma, Z.; Lin, H.; Liu, Y. $Rb_2CuSb_7S_{12}$: Quaternary Antimony-Rich Semiconductor Featuring a Three-Dimensional Open Framework and Exhibiting an Intriguing Photocurrent Response. *Inorg. Chem.* **2021**, *60* (13), 9263−9267.

(6) Pal, K.; Hua, X.; Xia, Y.; Wolverton, C. Unraveling the Structure-Valence-Property Relationships in $AMM'Q_3$ Chalcogenides with Promising Thermoelectric Performance. *ACS Appl. Energy Mater.* **2020**, *3* (3), 2110−2119.

(7) Pal, K.; Xia, Y.; He, J.; Wolverton, C. Intrinsically Low Lattice Thermal Conductivity Derived from Rattler Cations in an $AMM'Q_3$ Family of Chalcogenides. *Chem. Mater.* **2019**, *31* (21), 8734−8741.

(8) Pal, K.; Xia, Y.; Shen, J.; He, J.; Luo, Y.; Kanatzidis, M. G.; Wolverton, C. Accelerated discovery of a large family of quaternary chalcogenides with very low lattice thermal conductivity. *npj Computational Materials* **2021**, *7* (1), 82.

(9) Mansuetto, M. F.; Keane, P. M.; Ibers, J. A. Synthesis, structure, and conductivity of the new group IV chalcogenides, $KCuZrQ_3$ (Q = S, Se, Te). *J. Solid State Chem.* **1992**, *101* (2), 257−264.

(10) Maier, S.; Prakash, J.; Berthebaud, D.; Perez, O.; Bobev, S.; Gascoin, F. Crystal structures of the four new quaternary copper(I)-selenides $A_{0.5}CuZrSe_3$ and $ACuYSe_3$(A = Sr, Ba). *J. Solid State Chem.* **2016**, *242*, 14−20.

(11) Huang, F. Q.; Mitchell, K.; Ibers, J. A. New Layered Materials: Syntheses, Structures, and Optical and Magnetic Properties of $CsGdZnSe_3$, $CsZrCuSe_3$, $CsUCuSe_3$, and $BaGdCuSe_3$. *Inorg. Chem.* **2001**, *40* (20), 5123−5126.

(12) Liao, J. H.; Varotsis, C.; Kanatzidis, M. G. Syntheses, structures, and properties of six novel alkali metal tin sulfides: $K_2Sn_2S_8$, α-$Rb_2Sn_2S_8$, β-$Rb_2Sn_2S_8$, $K_2Sn_2S_5$, $Cs_2Sn_2S_6$, and Cs_2SnS_{14}. *Inorg. Chem.* **1993**, *32* (11), 2453−2462.

(13) McCarthy, T. J.; Ngeyi, S. P.; Liao, J. H.; DeGroot, D. C.; Hogan, T.; Kannewurf, C. R.; Kanatzidis, M. G. Molten salt synthesis and properties of three new solid-state ternary bismuth chalcogenides, β-$CsBiS_2$, γ-$CsBiS_2$, and $K_2Bi_8Se_{13}$. *Chem. Mater.* **1993**, *5* (3), 331−340.

(14) STOE & Cie GmbH (2020), X-area ver. 1.90, X-red ver. 1.65.2, X-Shape ver. 2.21, software package for collecting single-crystal data on STOE diffractometers, for image processing, scaling reflection intensities and for outlier rejection; Darmstadt, Germany.

(15) Sheldrick, G. SHELXT - Integrated space-group and crystal-structure determination. *Acta Crystallogr., Sect. A* **2015**, *71* (1), 3−8.

(16) Sheldrick, G. Crystal structure refinement with SHELXL. *Acta Crystallographica Section C* **2015**, *71* (1), 3−8.

(17) Dolomanov, O. V.; Bourhis, L. J.; Gildea, R. J.; Howard, J. A. K.; Puschmann, H. OLEX2: a complete structure solution, refinement and analysis program. *J. Appl. Crystallogr.* **2009**, *42* (2), 339−341.

(18) Hohenberg, P.; Kohn, W. Inhomogeneous Electron Gas. *Phys. Rev.* **1964**, *136* (3B), B864−B871.

(19) Kohn, W.; Sham, L. J. Self-Consistent Equations Including Exchange and Correlation Effects. *Phys. Rev.* **1965**, *140* (4A), A1133−A1138.

(20) Kresse, G.; Furthmüller, J. Efficiency of ab-initio total energy calculations for metals and semiconductors using a plane-wave basis set. *Comput. Mater. Sci.* **1996**, *6* (1), 15−50.
(21) Kresse, G.; Furthmüller, J. Efficient iterative schemes for ab initio total-energy calculations using a plane-wave basis set. *Phys. Rev. B* **1996**, *54* (16), 11169−11186.
(22) Blöchl, P. E. Projector augmented-wave method. *Phys. Rev. B* **1994**, *50* (24), 17953−17979.
(23) Perdew, J. P.; Ruzsinszky, A.; Csonka, G. I.; Vydrov, O. A.; Scuseria, G. E.; Constantin, L. A.; Zhou, X.; Burke, K. Restoring the Density-Gradient Expansion for Exchange in Solids and Surfaces. *Phys. Rev. Lett.* **2008**, *100* (13), 136406.
(24) Togo, A.; Tanaka, I. First principles phonon calculations in materials science. *Scripta Materialia* **2015**, *108*, 1−5.
(25) Dronskowski, R.; Bloechl, P. E. Crystal orbital Hamilton populations (COHP): energy-resolved visualization of chemical bonding in solids based on density-functional calculations. *J. Phys. Chem.* **1993**, *97* (33), 8617−8624.
(26) Deringer, V. L.; Tchougréeff, A. L.; Dronskowski, R. Crystal Orbital Hamilton Population (COHP) Analysis As Projected from Plane-Wave Basis Sets. *J. Phys. Chem. A* **2011**, *115* (21), 5461−5466.
(27) Baláž, M.; Zorkovská, A.; Urakaev, F.; Baláž, P.; Briančin, J.; Bujňáková, Z.; Achimovičová, M.; Gock, E. Ultrafast mechanochemical synthesis of copper sulfides. *RSC Adv.* **2016**, *6* (91), 87836−87842.
(28) Giggenbach, W. On the nature of the blue solutions of sulfur. *Journal of Inorganic and Nuclear Chemistry* **1968**, *30* (12), 3189−3201.
(29) Mansuetto, M. F.; Keane, P. M.; Ibers, J. A. Synthesis and Structures of the New Group IV Chalcogenides $NaCuTiS_3$ and $NaCuZrQ_3$ (Q = S, Se, Te). *J. Solid State Chem.* **1993**, *105* (2), 580−587.
(30) Kanatzidis, M. G.; Park, Y. Polychalcogenide synthesis in molten salts. Novel one-dimensional compounds in the potassium-copper-sulfur system containing exclusively S_4^{2-} ligands. *J. Am. Chem. Soc.* **1989**, *111* (10), 3767−3769.
(31) Park, Y.; Kanatzidis, M. G.; Kannewurf, C. R.; Degroot, D. C.; Schindler, J. $K_2Cu_5Te_5$, a Novel Mixed-Valence Layered Compound with Metallic Properties. *Angewandte Chemie International Edition in English* **1991**, *30* (10), 1325−1328.
(32) Yamashita, D.; Ishizaki, A. In situ measurements of change in work function of Pt, Pd and Au surfaces during desorption of oxygen by using photoemission yield spectrometer in air. *Appl. Surf. Sci.* **2016**, *363*, 240−244.
(33) Harwell, J. R.; Baikie, T. K.; Baikie, I. D.; Payne, J. L.; Ni, C.; Irvine, J. T. S.; Turnbull, G. A.; Samuel, I. D. W. Probing the energy levels of perovskite solar cells via Kelvin probe and UV ambient pressure photoemission spectroscopy. *Phys. Chem. Chem. Phys.* **2016**, *18* (29), 19738−19745.
(34) Morales-García, Á.; Valero, R.; Illas, F. An Empirical, yet Practical Way To Predict the Band Gap in Solids by Using Density Functional Band Structure Calculations. *J. Phys. Chem. C* **2017**, *121* (34), 18862−18866.
(35) Halasyamani, P. S.; Poeppelmeier, K. R. Noncentrosymmetric Oxides. *Chem. Mater.* **1998**, *10* (10), 2753−2769.
(36) Kang, S. K.; Tang, H.; Albright, T. A. Structures for d0ML6 and ML5 complexes. *J. Am. Chem. Soc.* **1993**, *115* (5), 1971−1981.
(37) Wheeler, R. A.; Whangbo, M. H.; Hughbanks, T.; Hoffmann, R.; Burdett, J. K.; Albright, T. A. Symmetric vs. asymmetric linear M-X-M linkages in molecules, polymers, and extended networks. *J. Am. Chem. Soc.* **1986**, *108* (9), 2222−2236.
(38) Welk, M. E.; Norquist, A. J.; Arnold, F. P.; Stern, C. L.; Poeppelmeier, K. R. Out-of-Center Distortions in d0 Transition Metal Oxide Fluoride Anions. *Inorg. Chem.* **2002**, *41* (20), 5119−5125.
(39) Wedler, H. B.; Wendelboe, P.; Power, P. P. Second-Order Jahn−Teller (SOJT) Structural Distortions in Multiply Bonded Higher Main Group Compounds. *Organometallics* **2018**, *37* (18), 2929−2936.
(40) Yan, Q.; Kanatzidis, M. G. High-performance thermoelectrics and challenges for practical devices. *Nat. Mater.* **2022**, *21* (5), 503−513.
(41) Gopal, E. S. R. *Specific Heats at Low Temperatures*; Springer: 1966.
(42) Tan, G.; Liu, W.; Chi, H.; Su, X.; Wang, S.; Yan, Y.; Tang, X.; Wong-Ng, W.; Uher, C. Realization of high thermoelectric performance in p-type unfilled ternary skutterudites $FeSb_{2+x}Te_{1-x}$ via band structure modification and significant point defect scattering. *Acta Mater.* **2013**, *61* (20), 7693−7704.
(43) Phillips, N. E. Heat Capacity of Aluminum between 0.1K and 4.0K. *Phys. Rev.* **1959**, *114* (3), 676−685.
(44) Zhao, L. L.; Lausberg, S.; Kim, H.; Tanatar, M. A.; Brando, M.; Prozorov, R.; Morosan, E. Type-I superconductivity in $YbSb_2$ single crystals. *Phys. Rev. B* **2012**, *85* (21), 214526.
(45) Slade, T. J.; Pal, K.; Grovogui, J. A.; Bailey, T. P.; Male, J.; Khoury, J. F.; Zhou, X.; Chung, D. Y.; Snyder, G. J.; Uher, C.; Dravid, V. P.; Wolverton, C.; Kanatzidis, M. G. Contrasting SnTe−$NaSbTe_2$ and SnTe−$NaBiTe_2$ Thermoelectric Alloys: High Performance Facilitated by Increased Cation Vacancies and Lattice Softening. *J. Am. Chem. Soc.* **2020**, *142* (28), 12524−12535.
(46) Zhang, C.; He, J.; McClain, R.; Xie, H.; Cai, S.; Walters, L. N.; Shen, J.; Ding, F.; Zhou, X.; Malliakas, C. D.; Rondinelli, J. M.; Kanatzidis, M. G.; Wolverton, C.; Dravid, V. P.; Poeppelmeier, K. R. Low Thermal Conductivity in Heteroanionic Materials with Layers of Homoleptic Polyhedra. *J. Am. Chem. Soc.* **2022**, *144* (6), 2569−2579.

https://doi.org/10.1021/acs.chemmater.2c02104
Chem. Mater. 2022, 34, 8389−8402